# A Deep Polarimetric Analysis of the Debris Disk HD 106906

by

Katie Crotts
B.Sc., University of Washington, 2017

A Thesis Submitted in Partial Fulfillment of the
Requirements for the Degree of

MASTER OF SCIENCE

in the Department of Physics and Astronomy

A Deep Polarimetric Analysis of the Debris Disk HD 106906

by

Katie Crotts
B.Sc., University of Washington, 2017

**Supervisory Committee**

---

Dr. Brenda Matthews, Co-Supervisor
(Department of Physics and Astronomy)

---

Dr. Ruobing Dong, Co-Supervisor
(Department of Physics and Astronomy)

## ABSTRACT

HD 106906 is a young, binary stellar system, located at ∼103.3 parsecs away in the Lower Centaurus Crux (LCC) group. This system is completely unique among known systems in that it contains an asymmetrical debris disk, as well as an 11 $M_{Jup}$ planet companion, at a separation of ∼735 AU. Only 4 other systems are known to contain both a disk and detected planet, where HD 106906 is the only one in which the planet has apparently been ejected. Furthermore, the debris disk is nearly edge on, and extends roughly from 70 AU to >500 AU, where previous polarimetric studies with HST have shown the outer regions to have high asymmetry. The presence of a planet companion sparks questions about the origin of this asymmetry. To better understand the structure and composition of the disk, deeper data have been taken with the Gemini Planet Imager (GPI), which we have used to perform a deep polarimetric study of HD 106906's asymmetrical debris disk. The data were taken in the H-band, and were supplemented with both J- and K1-band polarimetric data which have been obtained through one of GPI's Large and Long Programs (LLP). Polarimetry is important in the study of debris disks in scattered light, as it helps us constrain their dust grain characteristics, as well as allowing us to obtain high-contrast images. Modelling the disk, along with an empirical analysis of our data, supports a disk that is asymmetrical in surface brightness and structure, as well as a disk that is highly eccentric. These results will be discussed in terms of possible sources of asymmetry, such as dynamical interaction with the planet companion HD 106906b.

# Contents

# List of Tables

# List of Figures

ACKNOWLEDGEMENTS

I would like to thank:

**My family,** for their constant love and support, along with their tolerance of my sarcasm for years on end.

**Brenda Matthews,** for seeing something in me and allowing me to come to my full potential. Also, for just being an awesome advisor overall.

**The GPI Team,** for all of the immense help they gave me with this project.

**My partner Tyler Bates,** for always lifting me up when I'm down and for being my rock. The abundance of cute dog videos you send me are what get me through the day! Thank you for being in my life.

**My friends,** for always being there for me and for all the good times, truly making this an awesome journey. Shout out to Jaclyn Jensen for being an amazing friend and always helping to motivate me when I needed it. Second shout out to William Thompson for being a computer wizard and always willing to take the time to help me with my coding problems. You guys are the best!

*While it is always best to believe in oneself, a little help from others can be a great blessing.*
Uncle Iroh

# DEDICATION

To my friends and family. I could not have gotten here without you.

# Chapter 1

# Introduction

*The work done in this thesis will be published in Crotts et al. (2020), which will be submitted to the Astrophysical Journal. While I am lead author for this work, the observational data, MCFOST, and the GPI data reduction pipeline were obtained from collaborators.*

## 1.1 Debris Disks

As stars are born from massive molecular clouds, the conservation of angular momentum allows for a relatively thin disk of gas and dust to form around these young stars. These are the environments and materials that give rise to planetary systems, from smaller bodies such as asteroids and comets, all the way up to giant Jupiter-sized planets. While there are several theories as to how planets form, such as core accretion (Ormel & Klahr 2010; Levison et al. 2015), where small particles in a disk accrete to form larger bodies, and gravitational instability (Boss 1997), where over dense regions in a disk collapse, the details of planet formation are not yet fully understood. In recent years, however, this knowledge has become more accessible with the increasing number of discovered disks with planets, as well as directly imaged planets undergoing formation within a disk, such as with the system PDS 70 (Keppler et al. 2018; Müller et al. 2018). It is for this reason that observations of circumstellar disks themselves at different stages have become so important for better understanding these processes, as this is where they take place.

Early in their lifetimes ($\sim$first few million years), circumstellar disks are rich in both primordial gas and dust from their origin. This stage is called the protoplanetary disk stage, as this is the time at which it is believed the majority of planet formation takes place. However, over the next ~5-10 Myr, these disks will change as the dust forms planetismals/planets and the gas is dispersed through accretion onto the star, photo-evaporation, stellar winds, and other processes (Williams & Cieza 2011). Eventually there will be little to no gas left in the disk, and the majority of the small dust grains will have become a part of larger bodies. Once a planetary system has formed from its protoplanetary disk, the smaller rocky bodies which failed to become planets will create a new type disk, otherwise known as a debris disk.

While debris disks are typically not as large and bright as protoplanetary disks, making them harder to directly observe, they are still equally important to study. One of these reasons is due to the fact that the main characteristic of a debris disk is not just the lack of primordial gas and dust, but also the presence of secondary dust grains. Secondary dust grains differ from primordial dust grains in that they did not originate from the initial formation of the protoplanetary disk. Instead, they are a direct result from collisions between planetismals such as asteroids and comets within the disk. In short, the mere presence of a debris disk indicates the successful formation of bodies of at least several 100 to 1000 km in size. This can be confirmed as small dust grains should have been cleared out from stellar radiation pressure and winds on short timescales, however, their presence in debris disks indicates that small dust grains need to be constantly replenished. This process of colliding planetismals into smaller bodies down to sub-micron sized dust grains is called a *collisional cascade* (Matthews et al. 2014). In order for a collisional cascade to occur and continually produce smaller dust grains, planetismals need to have an efficient relative velocity to cause fragmentation upon impact, meaning that some sort of stirring mechanism is required to perturb their orbits.

There are several stirring mechanisms that could occur, such as late planetismal formation at large distances from the star (Kennedy & Wyatt 2014; Kenyon & Bromley 2008), interaction with the interstellar medium (ISM, Debes et al. 2009), close encounters with nearby stars (Kennedy et al. 2014), as well as planetary scattering (Kalas et al. 2015). The source of stirring may be determined by direct observation, as each of these mechanisms can affect the morphology and properties of the disk in slightly different ways, such as warps, eccentric disks, gaps, and spirals. Figure 1.1 shows the diversity in the debris disk structures as viewed in scattered and millimeter thermal light, where some of these features can be observed.

In any of these cases, the chances of creating an asymmetrical debris disk, in either

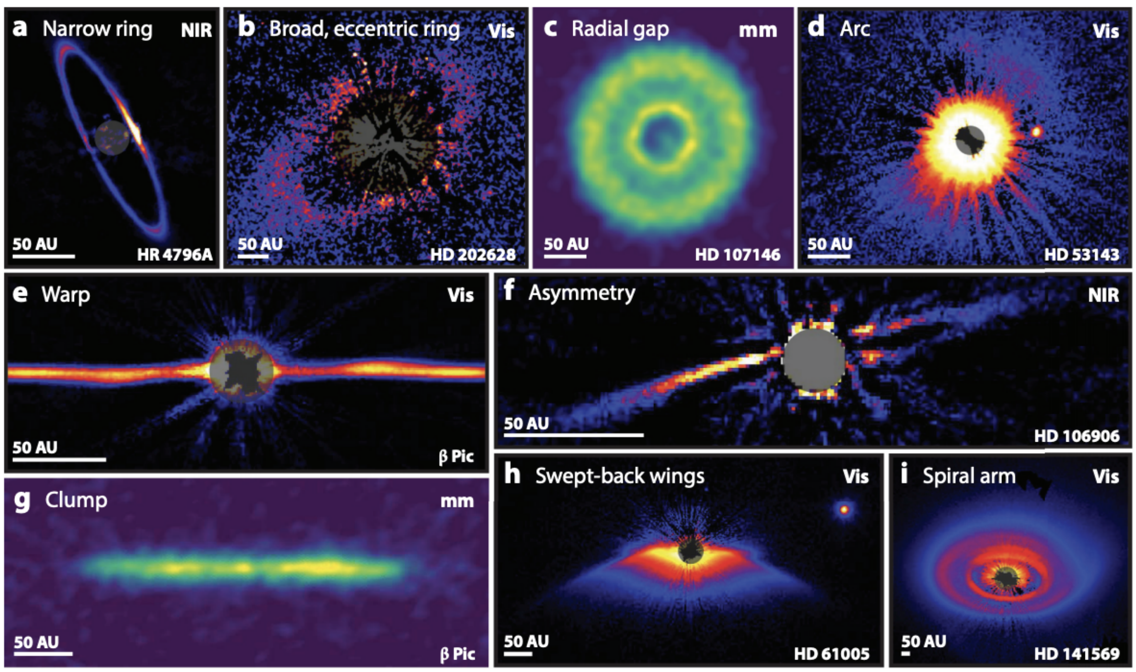


Figure 1.1: Diversity of debris disk structures observed in both scattered and millimeter thermal light. NIR=Near-Infrared, Vis=Visible, and mm=millimeter. Here, (f) is the system HD 106906, which is the focus of this Thesis. Figure taken from Hughes et al. (2018) with permission.

terms of brightness or morphology, are relatively high. For this reason, asymmetrical debris disks are especially interesting and make great candidates to study. By observing these types of disks, we can gain a better idea of their underlying dynamics, which in turn also gives us more insight into the architecture of exoplanetary systems. $\beta$ Pic is a good example of this, a system that contains both a warped debris disk and a detected planet companion within the inner disk (Lagrange et al. 2009). High resolution, multi-wavelength observations of the disk (Vandenbussche et al. 2010; Lagrange et al. 2012; Dent et al. 2014) have provided constraints on the detected planet's orbital properties (Wang et al. 2016). Additionally, it was demonstrated through two numerical models that the detected planet could be solely responsible for the disk's warp and overall morphology (Dawson et al. 2011; Nesvold & Kuchner 2015a), although research has also shown that more than one planet may in fact be needed to do this (Millar-Blanchaer et al. 2015; Apai et al. 2015).

While there are only a handful of cases of systems with known disks and planets, debris disk morphology can still be used to put constraints on undetected planets within and outside the disk. Many debris disks have ring like structures, meaning large cavities between the star and the disk are commonly present, and which may have been carved out by planets (Nesvold & Kuchner 2015b). In addition to the central cavity, some debris disks also exhibit gaps creating multiple rings. In both cases, these structures may be used to approximate the mass of the planet, for example, a possible gap which was found in the debris disk HD 107146 was used to determine that a planet of only a few Earth masses was necessary to open up such a gap (Ricci et al. 2014). Looking at larger scale morphology may also shed light on underlying planets, where a single, possibly eccentric planet has been shown to cause large asymmetries such as the "Needle", "Moth" and "Bar" (Lee & Chiang 2016) as seen in Figure 1.2.

These constraints are important as they give a broader insight into the distribution of different types of exoplanets. While the majority of exoplanets have been discovered through transit and radial velocity measurements, these methods are biased towards larger sized planets located closer to their host star, as can be seen in Figure 1.3. This begs the question as to whether or not smaller planets farther from their host star are really less common, are just less likely to be observed, or both. While statistical analyses have been attempted to further answer this question, as shown, debris disks provide a way to use direct observations to help fill in these gaps.

Due to the collisional nature of debris disks, studying the dust grain properties also gives us important information about these systems. For example, Spitzer spec-

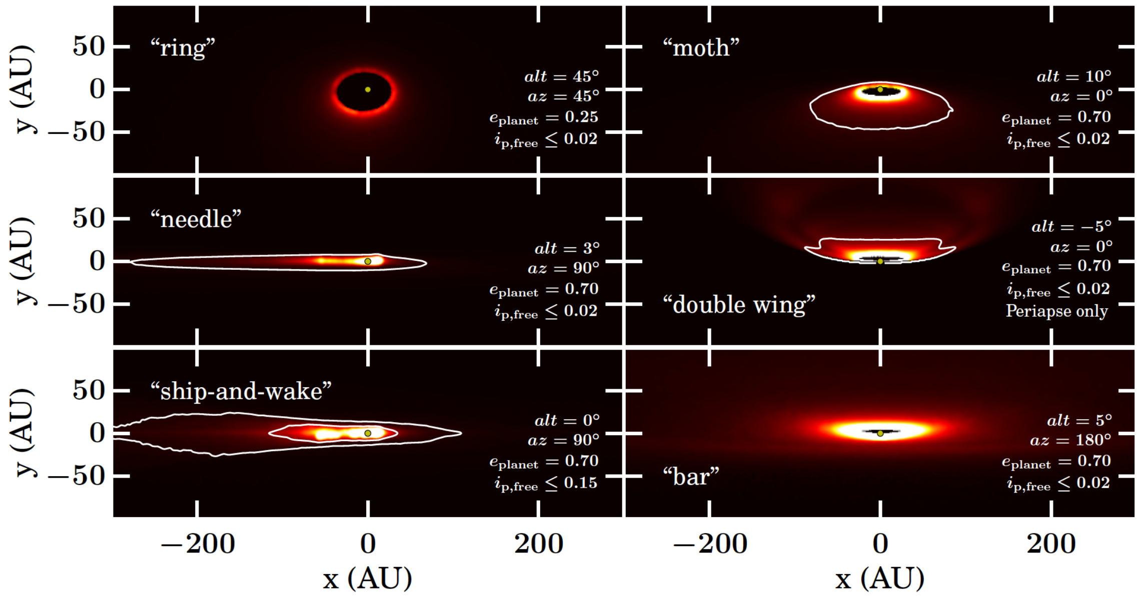


Figure 1.2: Debris disk morphologies as seen in scattered light. Models consist of a single eccentric planet, ring of parent bodies, dust grains and stellar radiation pressure. Figure taken from Lee & Chiang (2016) with permission.

troscopy of many debris disks has shown that dust composition is dominated by silicate with small amounts of refractories and water ices, very similar to dust in our Solar System (Olofsson et al. 2012; Mittal et al. 2015). Other studies have shown that the minimum dust grain sizes found in a sample of debris disks (1-10$\mu$m) are consistent with the blowout size (Pawellek & Krivov 2015), where dust grains below the blowout size should be dispersed due to radiation pressure from the star. However, deviations from these general results could indicate recent dynamical activity occurring. In the case of the asymmetrical debris disk, HD 111520, one side of the disk was found through modelling to have enhanced amounts of water ice, as well as a minimum dust grain size well below the calculated blowout size. This led to the conclusion that a recent collision between two icy bodies may be responsible for these dust grain features, as well as the brightness asymmetry of the disk (Draper 2018). The scenario of a recent collision could be said for many debris disks with asymmetries, however, indicating the importance of identifying possible stirring mechanisms, such as a known planet companion.

To summarize, the existence of debris disks indicates the successful formation of planetary bodies from a protoplanetary disk, as well as the occurrence of dynamical activity leading to a collisional cascade. Observing large samples of debris disks

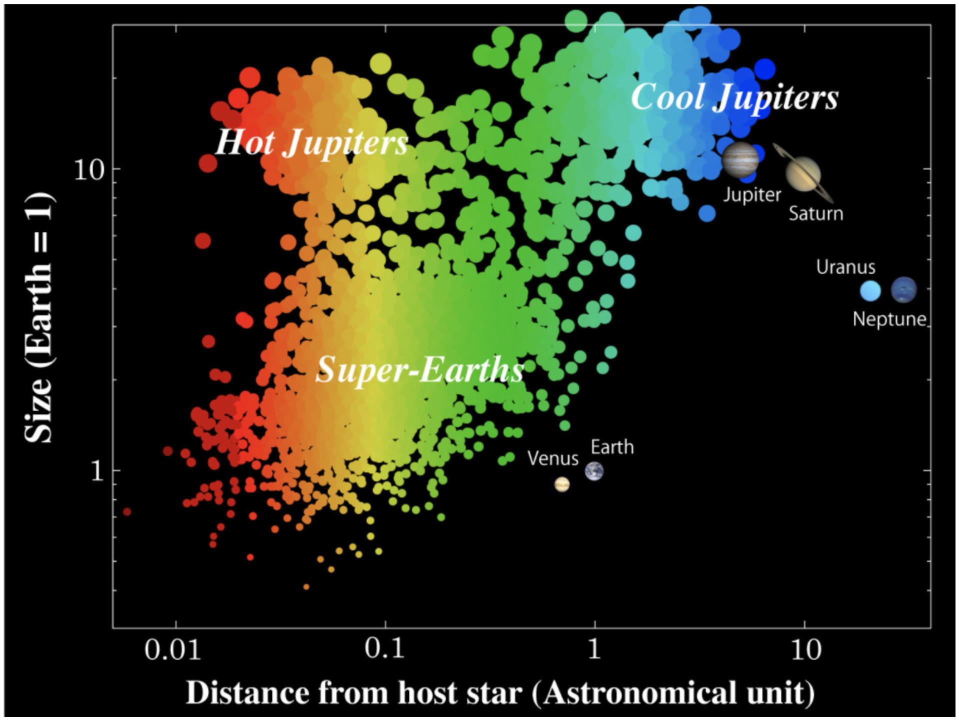


Figure 1.3: Discovered exoplanets plotted by Size vs. Distance from host star in AU (Source: www.exoplanets.org). Solar System objects are also plotted for reference.

has shown that this defining trait can cause a wide range of morphologies, asymmetries, and have a strong affect on dust grain properties. This in turn has allowed astronomers to put constraints on the planets shaping these systems, as well as have a deeper understanding of how exoplanetary systems evolve. This shows the importance of studying of debris disks, as they give us insight about the architecture and properties of planetary systems outside of our solar system.

## 1.2 Polarimetry and Direct Imaging

There are two ways in which debris disks are detected via imaging. 1) Through the fraction of light from the central star(s) which scatters off the dust grains. 2) Through the fraction of light from the central star(s) absorbed by the dust grains, which are then re-emitted as thermal emission. The scattering and emission behavior of dust grains highly depends on wavelength, where the observed light will be dominated by grains that are close in size to the wavelength being observed. To put this into context, while observations of debris disks at millimeter wavelengths trace the thermal emission from larger mm-sized dust grains, observations at optical and near-infrared (IR) wavelengths trace the scattered light off of smaller micron sized dust grains. For this reason, multi-wavelength observations are very important for having a complete understanding of the properties and distribution of dust grains in the disk, which provides information on the dynamical activity and stirring mechanisms occurring.

Focusing on scattered light observations at shorter wavelengths, a technique know as "direct imaging" is utilized. As the name suggests, this technique is used to directly image the scattered light from dust grains in the disk. These types of observations are crucial as they show detailed disk structure, as well as important information about the dust grain properties can be derived. For example, the scattered light from smaller dust grains is highly affected by the minimum dust grain size, which is typically on the order of one micron. Additionally, small dust grains are particularly good at polarizing light, meaning that part of each photon is absorbed, allowing for only light propagating along a certain axis to be scattered. Polarimetric observations of debris disks are especially useful as the polarization of light is strongly affected by the properties of dust grains. This includes composition, due to different molecules having differing refractive indices, as well as the porosity of the grains.

Observing debris disks in polarized light also has several advantages compared to total intensity (TI) observations. Because the light directly from stars is not polarized, they are automatically subtracted out from the data. This allows us to skip the additional step of point source flux (PSF) subtraction, which is needed for TI data in order to remove flux from the star, even in the presence of a coronagraph. While there are several PSF subtraction methods, in every case, a portion of light from the disk itself is also subjected to subtraction. Because this is not necessary for polarized observations, the issue of self-subtraction does not arise, allowing us to probe a more accurate representation of the disks relative brightness and structure.

There are four main polarization states, commonly known as the Stokes Vectors. These states are denoted as [I,Q,U,V], where I represents the TI, and the other three represent partial polarization states that differ in orientation and direction of rotation of the polarized light. The important vectors for observing debris disks in polarized light are Stokes Q and U, as they represent the linear polarization states. These two vectors are combined to create the radial components $Q_r$ and $U_r$, also known as the Stokes vectors in polar coordinates. For a circumstellar disk, $Q_r$ traces the polarized emission from the disk, while $U_r$ contains mainly noise. The definition for the radial state $Q_r$ can be seen in Eq. (3.3).

### 1.2.1 The Gemini Planet Imager

The Gemini Planet Imager (GPI, Macintosh et al. 2014) is a polarimeter and integral-field spectrometer located at the Gemini South observatory in Cerro Pachón, Chile. This instrument utilizes extreme adaptive-optics (ExAO), a technique that uses a deformable mirror to correct the distortion of incoming light due to atmospheric turbulence. This allows for high contrast imaging, making it ideal for exoplanet and debris disk observations which requires excellent resolution. GPI can also observe in both polarized and total intensity light, both of which are important for debris disk science.

GPI observes in the near-IR bands Y, J, H, K1, and K2, spanning a wavelength range of 0.9 to 2.4 microns. While this range may seem small, the scattering of light from small dust grains can change drastically over this range and therefore still impart important information about the properties of the dust grains in the disk. While GPI was primarily intended for the search and imaging of exoplanets, this has given way to a plethora of debris disk detections and observations, making this instrument fundamental to the debris disk science community.

## 1.3 HD 106906

From November 2014 to October 2018, GPI conducted its Exoplanet Survey (GPIES, PI B. Macintosh), which was an 860-hour campaign given to search roughly 600 stars for Jupiter-type planets, as well as a modest number of debris disks observable through scattered-light. Through this campaign, 185 debris disk targets were detected both through total scattered and polarized light (Esposito et al. 2020).

One of these disks is HD 106906 (HIP 59960), located at 103.3 parsecs away (Gaia Collaboration et al. 2018), and which was first discovered by Spitzer through an infrared survey of 25 stars in the Lower Centaurus Crux group (Chen et al. 2005). HD 106906 is an extremely unique and interesting system for several reasons. First, it consists of an eccentric, tight binary ($e=0.669\pm0.002$), with two F5V type stars (De Rosa & Kalas 2019). Secondly, it has an apparent ejected $11\pm2$ $M_{Jup}$ planet companion outside of the disk, at a separation of $735\pm5$ AU (Bailey et al. 2013; Daemgen et al. 2017). And finally, HD 106906 has a debris disk that features a brightness asymmetry, with a south-east (SE) extension that appears brighter than the north-west (NW) extension (Kalas et al. 2015, Lagrange et al. 2016).

This brightness asymmetry could result from a single or several scenarios. One, there is a stellocentric offset, causing an elliptic disk with one side of the disk closer to the star. Two, there is a difference in dust grain properties between the two sides, causing one side to scatter light more efficiently than the other. Three, dynamical activity is occurring, such as one or more of the stirring mechanisms mentioned in Section 1.1, perturbing the planetismals in the disk which contribute to collisional dust mass. Multi-wavelength observations could help distinguish between these different scenarios.

The Hubble Space Telescope (HST) and the Spectro-Polarimetric High-contrast Exoplanet REsearch instrument (SPHERE), both of which have larger fields of view than GPI, have also taken images of this system in the optical and near infrared. The results from HST have shown that the NW side of the disk halo seems to extends beyond 500 AU, creating a "needle" like structure (Kalas et al. 2015), which can be seen in Figure 1.4. On the other hand, this same feature is not observed for the SE extension, and does not appear at all in the near infrared as imaged with SPHERE (Lagrange et al. 2016), shown in Figure 1.5. Both sets of data also show that the position of the planet has a position angle ∼21-23 degrees from the NW extension. However, due to the wide separation of HD 106906b, its orbit has not been constrained.

The fact that HD 106906 is a tight binary, has a possibly ejected planet companion and has an asymmetrical debris disk, raises questions about whether or not HD 106906b is responsible for the disk's asymmetry. Previous work has shown that if HD 106906b indeed formed within the disk, it could have migrated inwards, and consequently been ejected through dynamical interactions with the binary (Rodet et al. 2017). While an in situ formation scenario for the planet is possible, the scattering scenario is favoured due to the lack of circumstellar gas at that distance and the formation time exceeding the lifespan of gas in a fiducial protoplanetary disk. If the scattering scenario were true, the planet may have also had dynamical interactions with the disk on its ejected path.

By studying the HD 109606's morphology and properties, we can gain a deeper understanding as to what mechanisms may have caused the disk's asymmetries, as well as compare to other disks with similar features. Analyzing observational data and modelling the disk over multiple wavelengths allows us to place constraints on both its density structural and dust grain properties.

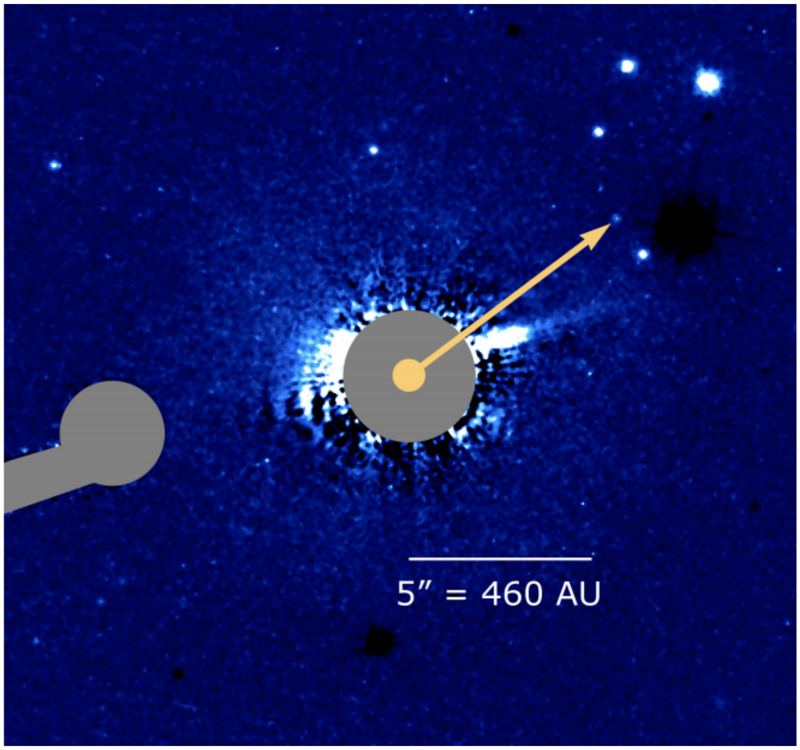


Figure 1.4: HST coronagraphic TI image of HD 106906 in the optical, where an extended feature in can be seen in the halo of the NW side of the disk. The arrow points towards the planet companion HD 106906b. Figure taken from Kalas et al. (2015) with permission.

## 1.4 Thesis Summary

This thesis will be presented over the course of several chapters. In **chapter 2**, I will discuss the polarimetric J-, H-, and K1-band data obtained of HD 106906 through GPI, as well as the data reduction process with the GPI Reduction Pipeline. I will then present the analysis of the data, and the derived observational results. **Chapter 3** will go over the modelling process of HD 106906, starting with an overview of the MCFOST disk model, followed by the method of using MCMC to constrain the density structural and dust grain properties of the disk, and finding a best fitting model. The final part of this chapter will go over the results, such as the distribution for each parameter and the best fitting models, obtained from this modelling procedure. **Chapter 4** will present an in-depth discussion of the results. This includes going into possible explanations for the derived dust grain properties, a comparison to other debris disks, limitations of our model, as well as a possible interaction with the planet HD 106906b. Finally, in **chapter 5** I will summarize my conclusions.

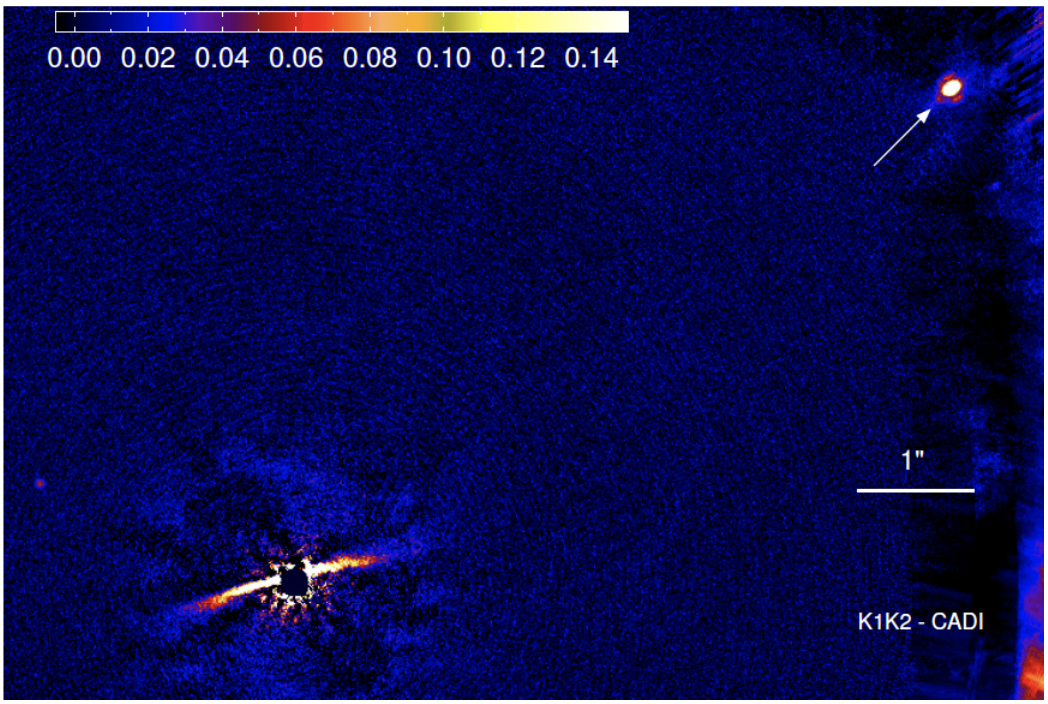


Figure 1.5: SPHERE TI image of HD 106906 in the near infrared. The arrow is again pointing towards the planet companion, HD 106906b. Figure taken from Lagrange et al. (2016) with permission.

# Chapter 2

# Data Reduction and Analysis

HD 106906 was observed with GPI as part of the original slate of debris disks in the GPIES survey. As for all GPIES disk targets, HD 106906 was observed only in H-band (Esposito et al. 2020). In this thesis we present deeper H-band data from GPI. These observations were given longer total exposure times (hence "deep") compared to the pol data presented in Kalas et al. (2015), and therefore had more telescope field rotation, leading to a higher S/N. In addition, we supplement this deep H-band data with new J- and K1-band GPI data, giving a total wavelength coverage of approximately 1.12 to 2.19 microns ($\mu$m). Further information about these observations are presented in the following section 2.1.

Section 2.2 covers the general process of reducing the data to achieve our final images in each band. We describe the methods of image analysis that significantly reduce the amount of instrumental noise in the data and enhance the disk detection. Once we have our final images, we can then use them to analyze the relative brightness and structure of the disk across all three bands. This includes measuring the vertical height of disk, as well as the peak surface brightness, giving us a better look at the disk's overall morphology.

## 2.1 GPI Observations

We have obtained deeper polarimetric data of HD 106906 in the H-band (peak $\lambda \sim$1.647 $\mu$m) from GPIES. In addition, we have also obtained J (peak $\lambda \sim$1.235$\mu$m) and K1-band (peak $\lambda \sim$2.048$\mu$m) data from one of GPI's Large and Long Programs (LLP), led by principle investigator (PI) Christine Chen. The H-band data were observed June 30$^{th}$, 2015, using GPI's spectroscopic (H-Spec) and polarimetric (H-Pol) modes. The J- and K1-band were observed over a four day period from March 24$^{th}$ through the 28$^{th}$ of 2016, again in spectroscopic (J-Spec and K1-Spec) and polarimetric (J-Pol and K1-Pol) modes. In this study, we will focus on only the polarimetric data. Further details about the polarimetric observations can be found in Table 2.1.

| Mode | Band | Date | $t_{exp}$ | N | $\Delta$PA (deg) | MASS Seeing |
|---|---|---|---|---|---|---|
| Pol | H | 2015 Jul 01 | 59.65 | 43 | 20.3 | 0.45″ |
| Pol | J | 2016 Mar 26 | 59.65 | 54 | 35.2 | 0.79″ |
| Pol | K1 | 2016 Mar 28 | 88.74 | 40 | 36.5 | 1.33″ |

Table 2.1: Details of observations with GPI for each band. $t_{exp}$ = the exposure time for each frame, N = the number of frames, $\Delta$PA = the total Parallactic Angle.

## 2.2 Data Reduction

Each of these sets of data were reduced through the GPI Data Reduction Pipeline (Perrin et al. 2014) which we breifly summarize here. In GPI's polarization mode, a pair of spots is created by each lenslet, representing both orthogonal polarization states Q and U. The first step in the reduction process is to create 3-dimensional cubes from the raw data, where the three dimensions contain an image for each orthogonal polarization state. To do this, the raw data are run through the GPI Pipeline using the Basic Polarization Sequence (From Raw Data) recipe. In this step, a spot calibration file is used to identify the pair of spots corresponding to each lenslet. The raw data are dark subtracted, bad pixel corrected and cleaned of correlated detector noise, where they are then combined into polarization data cubes. Finally, the position of the star is found by measuring a set of fiducial satellite spots (Wang et al. 2014).

Next, a re-calibrated radial Stokes cube is created using the pipeline's Basic Polarization Sequence (From podc cubes) recipe. In this step, the instrumental polarization is measured from the apparent stellar polarization in each datacube, which is then subtracted from each cube (Millar-Blanchaer et al. 2015). Next, the satellite-spot-to-star flux is measured in order to determine a photometric calibration factor. After this measurement, the 3-D cubes are combined to create a single radial Stokes image, consisting of Stokes [I,$Q_r$,$U_r$,V]. Finally, using the stellar magnitude and photometric calibration factor in each filter, the J- and K1-band data were calibrated from ADU coadd$^{-1}$ to Jy arcsec$^{-2}$. We find a calibration factor of $1.7266\times10^{-8}$ Jy/(ADU/coadd) with 3.015% uncertainty for the K1-band, and $1.8051\times10^{-8}$ Jy/(ADU/coadd) with 7.651% uncertainty for the J-band.

For the H-band data, a slightly different approach was used to calibrate the image from ADU coadd$^{-1}$ to Jy arcsec$^{-2}$, where instead of going through the GPI pipeline, a photometric calibration factor of $6.555\times10^{-7}$ Jy/(ADU/coadd) was used, which was derived in Esposito et al. (2020). The final images in each filter can be seen in Figure 2.1, where the left column represents the data in $Q_r$, and the left column represents the data in $U_r$. Surface brightness is in units of mJy arcsec$^{-2}$.

## 2.3 Observational Results

As seen in Figure 2.1, a brightness asymmetry can be observed in all three bands, where the SE extension is brighter than the NW extension. By eye this asymmetry seems to be most prominent in the H-band, whereas the asymmetry is slightly more subtle in the J- and K1-band. Figure 2.2 shows a closer look at the disk in each band, smoothed with a Gaussian ($\sigma = 1$), and overlaid with contours to give a better visual representation of the surface brightness features.

Additionally, we created noise maps using the standard deviation of $U_r$ in each wavelength, which should contain mainly noise and little to no disk signal. This noise map is created by evaluating the noise in 1-pixel wide annuli centered around the star. By dividing this noise map from our $Q_r$ images, we can create a Signal-to-Noise (S/N) image for each wavelength, which can be seen in Figure 2.3. Comparing the S/N between each band, we find that the H-band has the highest S/N, while J-band has the lowest.

### 2.3.1 Vertical Height

To better quantify the structure of the disk, we first measured the vertical height or FWHM of the disk in the H-band, due to its high S/N, as a function of distance from the star. To do this we first rotate our image so that the disk is horizontal. Next, we measure the surface brightness along vertical cross-sections of the disk, at various radial separations from the star until the whole disk has been covered. We then fit a Gaussian to each vertical brightness profile using Equation (2.1), where the FWHM can then be extracted from $\sim2.35\sigma$. The results can be seen in Figure 2.4, where

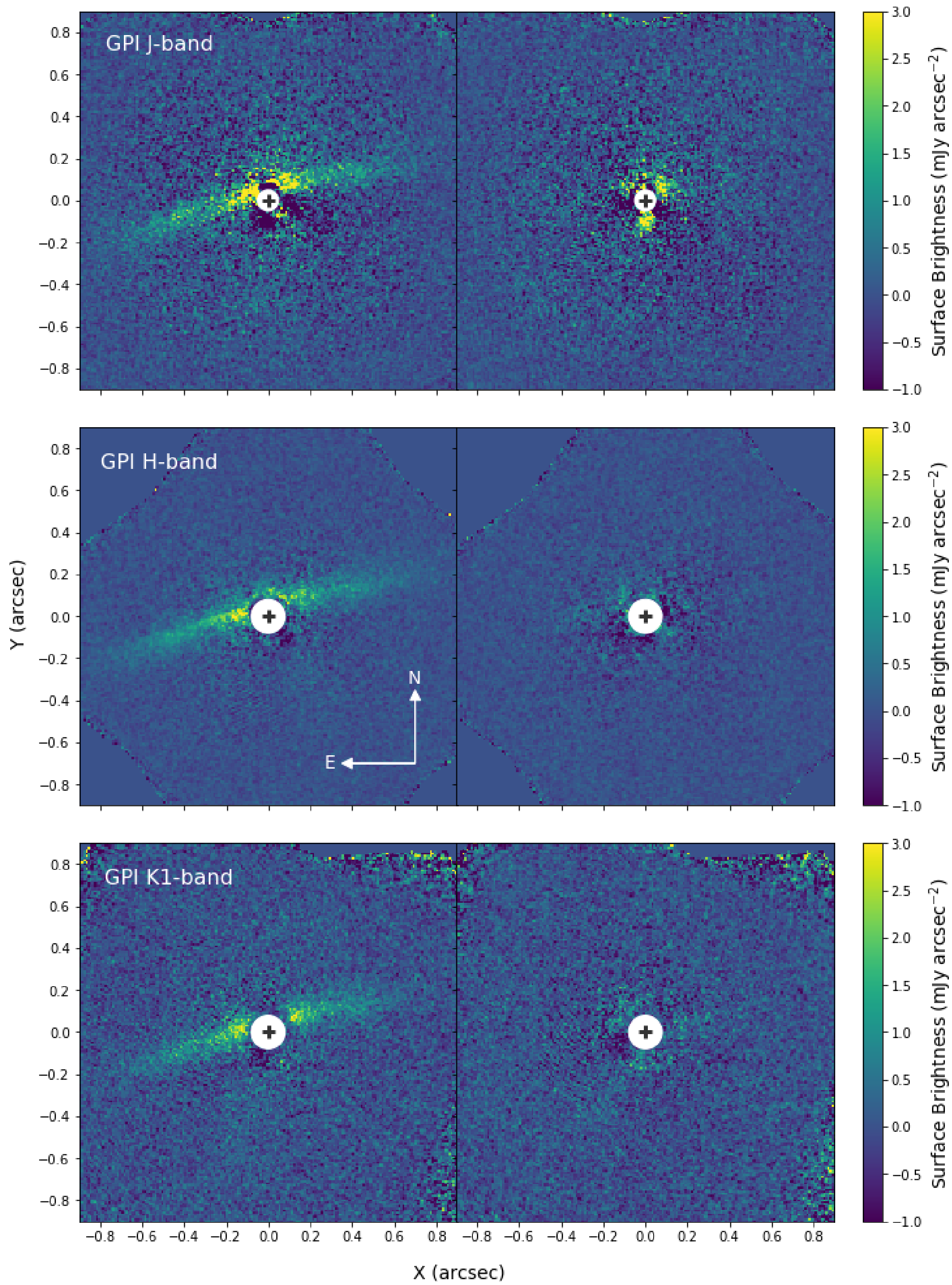


Figure 2.1: HD 106906 in J-, H- and K1-band polarized light as taken with GPI. **Left column** depicts the disk in $Q_r$. **Right column** depicts the disk in $U_r$. Surface brightness are in units of mJy arcsec$^{-2}$.

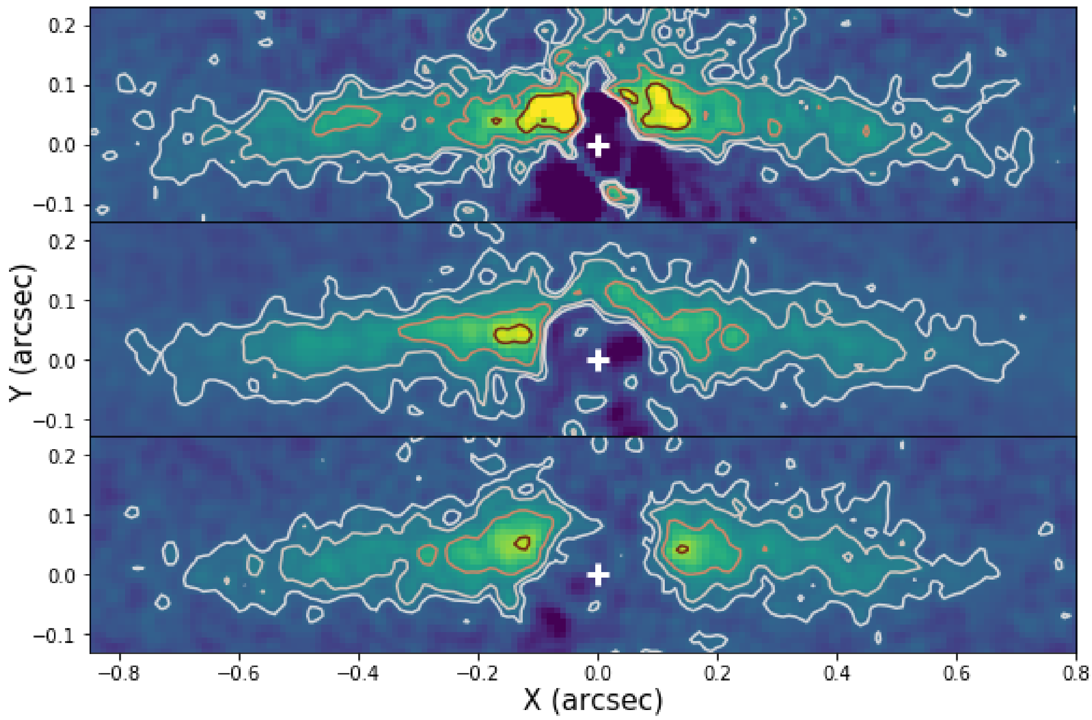


Figure 2.2: J-, H- and K1-band data, overlaid with surface brightness contours. Scaling is the same as in Figure 2.1. Contours represent a surface brightness of 0.3, 0.6, 1.2 and 2.4 mJy/arcsec$^2$.

both the FWHM and the distance from the star are in arcseconds. Error bars are taken from fitting of the Gaussian to the data.

$$g(x) = a\exp\left[\frac{-(y-y_0)^2}{2\sigma^2}\right] + b \tag{2.1}$$

On both sides we are able to measure the FWHM of the disk out to $\sim 0.8''$, meaning there is no significant asymmetry in radial extent. This agrees with the findings in Kalas et al. (2015), as they also found the disk in polarized light to be radially symmetric. The back side of the disk is identified via a significant increase in the FWHM, as the dramatic increase in width is from contributing scatter from the back side of the disk. We find this increase in back scatter on either side at $\sim 0.34''$, or 35.12 AU. The fact that this occurs in the same location across the disk could suggest that the inner disk is also quite symmetric; however, due to the high inclination of the disk, the FWHM is not a great indicator of the inner disk location. We also find that

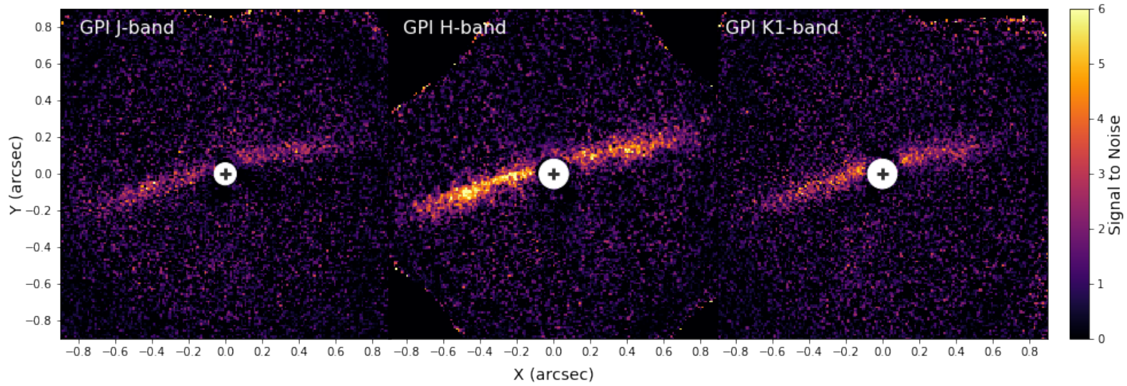


Figure 2.3: S/N plots for HD 106906 in J-, H- and K1-bands. Note that H-band has the highest S/N.

looking at the weighted mean FWHM between the two sides, shown by the dashed green and grey lines in Figure 2.4, the NW extension has a slightly larger vertical height on average (0.12″ compared to 0.11″ on the SE side). Both of these values are also about ∼8-15% less than the values measured in Kalas et al. (2015), as they measure a FWHM of ∼0.13″. Besides this, there does not seem to be any significant trends in the FHWM as the distance from the star increases.

### 2.3.2 Surface Brightness

For this section, we calculated the peak surface brightness profile in each wavelength. This is done by finding the peak brightness along the spine of the disk. After rotating the disk to be horizontal, we then find the max surface brightness along vertical slices. The peak surface brightness is finally binned by 3-pixels along the horizontal axis and averaged. These results can be found in Figure 2.5, showing the peak surface brightness in mJy arcsec$^2$ as a function of separation from the star in arcseconds. The error bars are calculated from the noise map in each filter.

Looking at the relative peak surface brightness between each band, we confirm that there is a slight brightness asymmetry in all three wavelengths. Comparing the average peak surface brightness between the two sides within <0.34″, we find a NW/SE ratio of 0.75±0.22 in the H-band, 0.80±0.37 in the J-band and 0.82±0.31 in the K1-band. This confirms that the brightness asymmetry is greatest in the H-band within this region, robustly due to its high S/N, however, this also shows that the asymmetry is not that extreme in polarized light considering a ratio of 1 lies within the ranges for the J- and K1-bands. We also detect a bright NW feature in

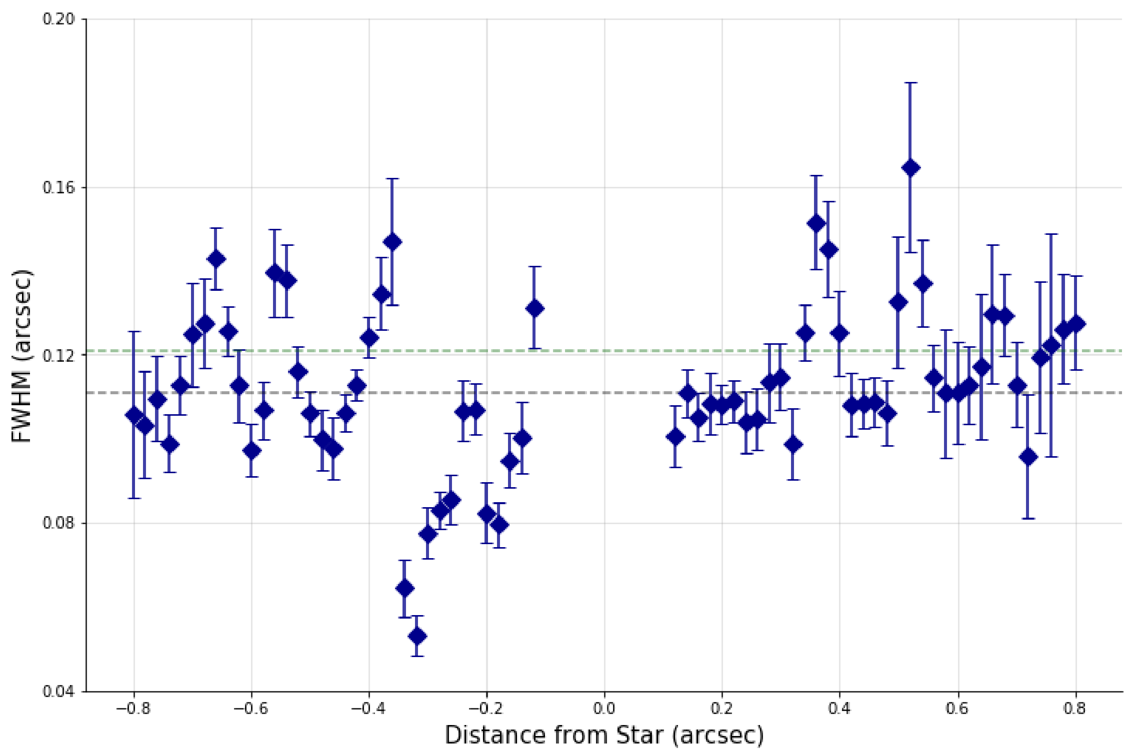


Figure 2.4: H-band FWHM profile of the disk as a function of distance from the star in arcseconds. The weighted mean FWHM of the SE extension is represented with the grey dashed line, and likewise with the green dashed line for the NW extension.

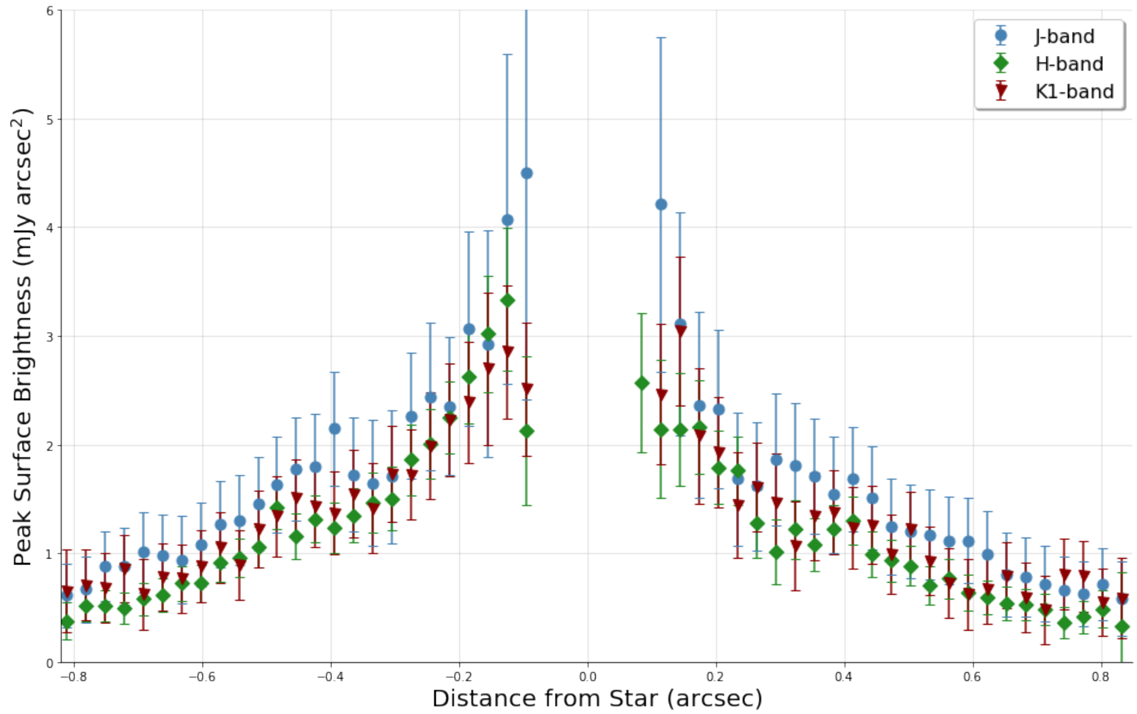


Figure 2.5: Peak surface brightness in each band along the disk as a function of distance from the star in arcseconds. Error bars represent $1\sigma$ uncertainties.

the K1-band at 0.15″, although it is within $1\sigma$ of the surface brightness of the SE extension in the same location. From 0.4″ to 0.5″, the brightness asymmetry peaks for the J- and K1-band with a measured NE/SE brightness ratio of 0.70±0.30 and 0.78±0.32 respectively, while increasing slightly in the H-band at 0.80±0.21. From here, the asymmetry decreases, to the point where past ∼0.6″ an asymmetry is no longer detected in any of the three bands.

We find the disk to have the highest median brightness in the J-band, although it also has the highest noise. On the other hand, the surface brightness is lowest in the H-band over all, except closest to the star in the SE extension. Towards the outer edge of the disk, >0.6″, the difference in the peak surface brightness between each wavelength is marginal. This being said, the surface brightness in all three bands are within $1\sigma$ of each other, making the comparison an approximation based on the median peak surface brightness.

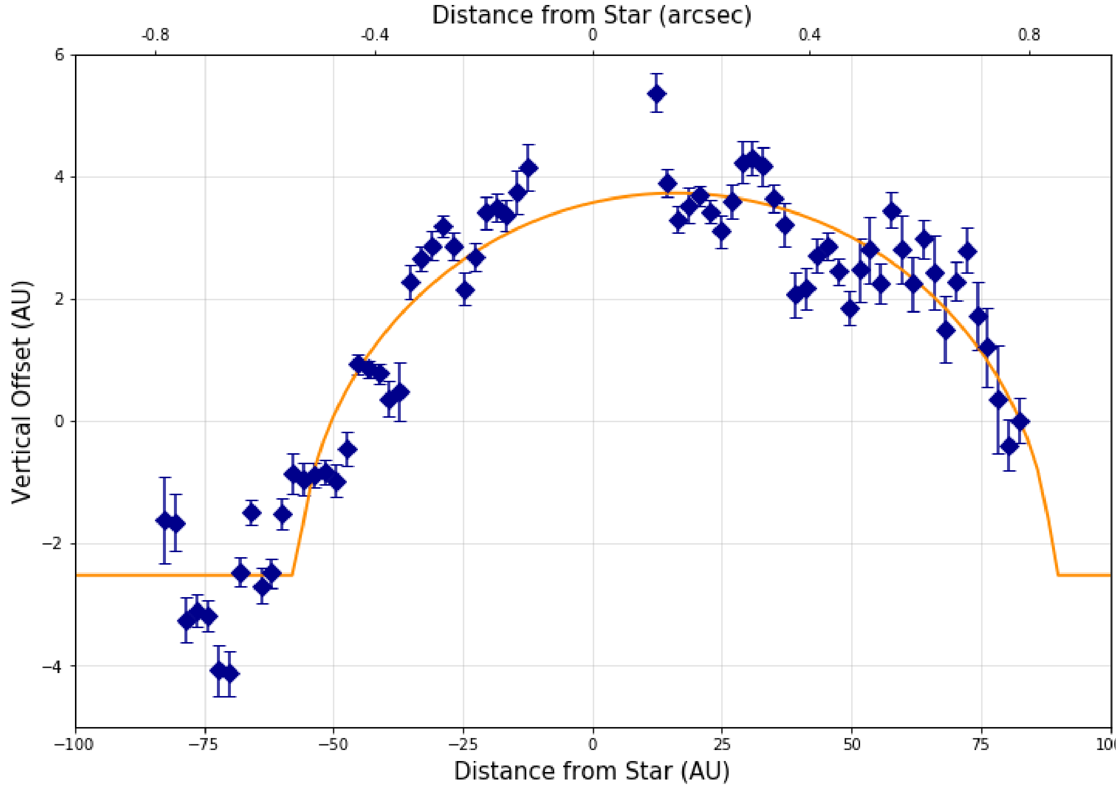


Figure 2.6: Vertical offset between the spine of HD 106906's disk, relative to the star, as a function of radial separation shown in AU and arcseconds. The orange line represents the inclined ring model that best fits the spine.

### 2.3.3 Vertical Offset

While the FWHM profile and the surface brightness profile don't exhibit strong asymmetries, fitting the spine of the disk may be more telling. The spine of the disk refers to where the peak surface brightness, along the disk, is located relative to the star in the vertical direction. To measure this, we refer back to our Gaussian fitting, where the spine location is related to the mean value of the Gaussian. We can then compare the vertical offset between the spine location and the star as a function of radial separation. These results can be seen as the blue data points in Figure 2.6, where the error bars are taken from the Gaussian fitting. At first glance, the vertical offset looks to be asymmetric on either side, where past 100 AU ($\sim 0.5''$) the vertical offset dips and stays below 0 in the SE extension, where this is not the case for the NW extension.

To investigate this asymmetry further, we generate a simple inclined ring model, where the ring radius ($R_d$), inclination ($i$), position angle (PA), as well as a disk offset in the x and y directions ($\delta_x$ and $\delta_y$) are kept as free parameters. A best fitting model is then found by using the method MCMC, which will be discussed in more detail in Chapter 3. Our best fitting model can be seen in Figure 2.6 as the orange line. Through this modelling we find $R_d = 72.70^{+2.55}_{-1.29}$ AU, $i = 85.07^{+0.15}_{-0.16}$ degrees, and PA $= 103.67^{+0.16}_{-0.30}$ degrees, where our inclination and PA are consistent with those derived in Kalas et al. (2015). More interestingly, we find $\delta_x = 16.13^{+2.73}_{-1.27}$ AU, and $\delta_y = -2.52^{+0.22}_{-0.32}$ AU, which implies a large eccentricity approaching $\sim$0.5. If this is true, due to the offset being towards the SE extension, it would most likely explain the brightness asymmetry that we observe. While modelling the spine suggests an inherently asymmetrical and eccentric disk, further analysis and ellipse fitting will be needed to further probe the eccentricity and disk orientation.

## 2.4 Summary

Using the GPI Reduction Pipeline, we perform data reduction on our obtained polarimetric H-band, J- and K1-band observations. Using the final calibrated data reductions, we were able to perform an analysis on the surface brightness and morphology of the disk. We first calculated the S/N of each band and found that the H-band had the highest S/N, while the J-band had the lowest S/N. Due to the high S/N of the H-band, we use this observation to measure the vertical height or FWHM of the disk as a function of radial separation from the star. We find that the NW extension has a slightly higher weighted mean FWHM compared to the SE extension, as well as the FWHM is measured out to about 0.8″, therefore making the two sides comparable in radial extent. By measuring the peak surface brightness along the disk, we confirm a brightness asymmetry in all three bands. This brightness asymmetry is most notable in the H-band within 0.34″, while being more subtle in the J- and K1-band. Where as we find that brightness asymmetry peaks from 0.4″ to 0.5″ for the J- and K1-band, while increasing slightly in the H-band. Past 0.6″, a brightness asymmetry is no longer detected. Finally, while the FWHM profile and peak surface brightness profile don't exhibit strong asymmetries, by fitting the spine of the disk, our results indicate significant offsets in both the x and y directions which would give the disk an eccentricity approaching $\sim$0.5. While fitting an ellipse is needed to probe the disk eccentricity and orientation further, this points to the disk truly being asymmetrical.

# Chapter 3

# Modelling of HD 106906

While analyzing the data directly is important for understanding the overall morphology of the disk, we can probe the properties of the disk further via modelling. There are a number of different modelling tools that have been created specifically to model circumstellar disks. To do this, the majority utilize what is known as Monte Carlo radiative transfer, a method which keeps track of each photon emitted from the central star(s) and their following interactions with the dust, such as through scattering and absorption. By creating scattered light images of model disks with such codes, we can then compare with our scattered light observations, and analyze whether or not the model is a good fit depending on how well it matches the data. This can be evaluated visually, looking at the residual between the model minus the data, and numerically, such as calculating the chi-squared parameter.

Finding a good fitting model requires a lot of adjustment of many different parameters, and therefore the creation of many models, which can be extremely time extensive and tedious to do by hand. Luckily there are computational methods that can be used to do this in a more efficient way. One of these methods is Markov Chain Monte Carlo (MCMC), which samples an entire given range for each parameter specified, in order to find a best fitting model along with a probability distribution. We utilize this method in an attempt to better constrain the properties of the HD 106906 disk, first modelling the density structure of the disk, followed by modelling the dust grain properties. In this chapter, we discuss in more detail the modelling code used for this analysis, along with our process of using MCMC to constrain the disk's properties, and then finally our results.

## 3.1 Debris Disk Model

MCFOST is a 3-D radiative transfer code, mainly designed to model circumstellar disks around young objects (Pinte et al. 2006). For our models, the "debris disk" option is chosen within MCFOST, which defines the volume profile as

$$\rho(r,z) \;\propto\; \frac{\exp\left(-\left(\frac{|z|}{h(r)}\right)^{\gamma_{\rm vert}}\right)}{\left[\left(\frac{r}{Rc}\right)^{-2\alpha_{\rm in}} + \left(\frac{r}{Rc}\right)^{-2\alpha_{\rm out}}\right]^{1/2}}. \tag{3.1}$$

$$\mathrm{h(r)} \;=\; \mathrm{H_0}\left(\frac{\mathrm{r}}{\mathrm{R_0}}\right) \tag{3.2}$$

In Equation (3.1), $r$ is the radial distance from the star in the plane of the disk, $R_c$ is the critical radius that defines where the surface density exponents $\alpha_{in}$ changes to $\alpha_{out}$ (Augereau et al. 1999). In addition, $z$ is the height above the disk mid-plane, *h(r)* describes the scale height profile, with a vertical exponent of $\gamma$. Equation (3.2) defines *h(r)*, where $H_0$ is the scale height at radius $R_0$.

For the dust grain properties Mie theory is used, where the dust grains are assumed to be spherical. This of course is not realistic and has implications that will be discussed in Chapter 4. However, for now, this assumption allows for easy and fast scattering computations. In addition, the dust grain size follows a power law distribution of $dN(a) \propto a^{-q}da$, where $a_{\rm min}$ is the minimum dust grain size up to a size of 1000 $\mu$m or 1 mm, and $q$ is the power law for the dust grain size distribution, denoted in this thesis as $a_{exp}$. We also explore dust composition, looking exclusively at the volume fractions of astro-silicates, amorphous carbon and water ice. The optical indices for each material are obtained from literature (Si, Draine & Lee 1984; aC, Rouleau & Martin 1991; $H_20$, Li & Greenberg 1998). These compositions are chosen as they are common to those observed in debris disks, as well as used in modelling of other disks.

### 3.1.1 Modelling Process

MCFOST is called within a Python function, which then creates a model using a parameter file, at a user specified wavelength. For our purposes, the wavelengths chosen were the peak throughput of each filter (J, H, K1), hence 1.235 $\mu$m, 1.647 $\mu$m, and 2.048 $\mu$m. This results in a 4-dimensional fits image, which includes the final model in the Stokes I, Q, U and V intensities. After each model is created, it is then prepared to be compared to the data. First, each model is converted to Stokes $\mathrm{Q_r}$, using the Equations (3.3) and (3.4).

$$\mathrm{Q_r} = \mathrm{Q} \cdot \cos(2\phi) + \mathrm{U} \cdot \sin(2\phi) \tag{3.3}$$

$$\phi = \tan^{-1}\left[\frac{(x - x_*)}{(y - y_*)}\right] \tag{3.4}$$

For Equations (3.3) and (3.4), Q and U represent the Stokes Q and U outputs from MCFOST, x and y are the locations of each pixel, while $\mathrm{x}_*$ and $\mathrm{y}_*$ represents the pixel location of the central star.

After each model has been converted to $\mathrm{Q_r}$, if the star is defined to have an offset (for an asymmetrical disk), the image is then shifted so that the star is relocated to the center of the image. This is important, as the GPI Pipeline automatically centers the star during the data reduction process. Once the star is at the center, the model is then convolved with a GPI PSF in the corresponding filter. Finally, the model is converted from W/m$^2$/pixel to Jy/arcsec$^2$.

## 3.2 MCMC Analysis

To determine the most likely values for the parameters that will be explored, the models must be compared to the data. To do this, the Python package *emcee* is utilized (Foreman-Mackey et al. 2013). Emcee uses MCMC, which is a type of statistical analysis, to determine the mostly likely values for each parameter, and thereby find a best fitting model.

### 3.2.1 Model Parameters

Initially, the H-band data are modelled alone, as these data have the highest S/N. The disk is modelled with a stellocentric offset parameter, to see whether or not this is enough to match the disks brightness asymmetry, as implied by our data analysis.

To begin with, the parameters that would most strongly affect the disk brightness are kept constant; these include dust grain properties such as the minimum grain size and composition. This is done to limit parameter space, and therefore speed up computation time. Instead, properties that are related to the density structure of the disk are allowed to vary over a range of priors. A list of density structural parameters, the initial value for each, and their prior range can be viewed in Table 3.1.

| Param. | Initial Val. | Limits |
|---|---|---|
| $H_0$ [AU] | 5.0 | [1, 10] |
| $\gamma$ | 2.0 | [0.1, 3] |
| $R_c$ [AU] | 100 | [50, 200] |
| $\alpha_{in}$ | 1.0 | [0.5, 15] |
| $\alpha_{out}$ | -1.0 | [-5, -0.5] |
| $x_*$ [AU] | 0.0 | [-40, 40] |
| $z_*$ [AU] | 0.0 | [-10, 10] |

Table 3.1: The density structural parameters chosen to be constrained, along with the initial value and prior limits chosen for MCMC analysis.

| Param. | Initial Val. | Limits |
|---|---|---|
| $M_{dust}$ [$M_\oplus$] | 0.033 | [0.00033, 3.33] |
| porosity | 0.5 | [0, 1] |
| $V_{Si}$ | 0.5 | [0, 1] |
| $V_{aC}$ | 0.5 | [0, 1] |
| $V_{H_20}$ | 0.5 | [0, 1] |
| $a_{min}$ [$\mu$m] | 1.5 | [0.3, 4] |
| $a_{exp}$ | 3.5 | [2, 6] |

Table 3.2: The dust grain parameters chosen to be constrained, along with the initial value and prior limits chosen for MCMC analysis.

As mentioned previously, $H_0$ is the scale height at the reference radius $R_0$, $\gamma$ is the vertical profile exponent, $R_c$ is the critical radius, $\alpha_{in}$ and $\alpha_{out}$ are the surface density exponents. Finally, $x_*$ and $z_*$ are the star's position from the center in the x and z directions, measured in AU. In 2d space, $x_*$ represents the star's position in the horizontal direction, and $z_*$ represents the star's position in the vertical direction. Important structural parameters such as inclination and position angle were not looked at in this analysis, as they are already well defined from previous work to be ~85 degrees and ~104 degrees, respectively (Lagrange et al. 2016; Kalas et al. 2015), as well as from our own analysis in Section 2.3.3. Therefore, we do not include them in order to reduce the parameter space to be constrained.

Following the modelling of the density structure, these parameters are held constant, and the dust grain parameters are then modelled. We first model the dust grain parameters with the H-band only due to its high S/N. This is then followed by modelling all three wavelengths together, where the SE and NW extensions are modelled separately, in the hopes of better constraining these parameters and to probe whether or not the two sides of varying dust grain properties. A list of the dust grain parameters, the initial value for each, and their prior range can be viewed in Table 3.2.

Here, $M_{dust}$ is the total dust mass of the disk in Earth masses, porosity defines how fluffy or compact the dust grains are. $V_{Si}$ is the volume fraction of astronomical silicate, while $V_{aC}$ is the volume fraction of amorphous carbon, and $V_{H_20}$ is the volume fraction of water ice. Finally, $a_{min}$ is the minimum dust grain size, and $a_{exp}$ is the power law for the distribution of dust grain sizes. For simplicity, the dust compositions (Si, aC, and $H_20$) are set to be physically joint within each dust grain, in that the three compositions make up one dust grain species.

### 3.2.2 MCMC Process

For each run, 200 walkers are deployed to explore the parameter space, starting at the initial values as stated in Tables 3.1 and 3.2. These walkers move around freely in order to find the max log likelihood values for each parameter, as well as their posterior distributions. This occurs for up to several thousand iterations until the parameters have either clearly converged, or the log likelihood for the walkers is no longer increasing.

## 3.3 Results

### 3.3.1 H-Band Only

For the MCMC analysis of the density structural parameters, emcee was allowed to run for about 10 days, until well after convergence to make sure that we had the best

| Param. | Max Lk. | 16% | 50% | 84% |
|---|---|---|---|---|
| $H_0$ [AU] | 3.78 | 4.07 | 4.34 | 4.38 |
| $\gamma$ | 0.66 | 0.708 | 0.715 | 0.723 |
| $R_c$ [AU] | 74.89 | 68.92 | 72.21 | 75.31 |
| $\alpha_{in}$ | 1.55 | 0.79 | 1.03 | 1.32 |
| $\alpha_{out}$ | -2.40 | -2.34 | -2.26 | -2.16 |
| $x_*$ [AU] | -4.88 | -3.63 | -3.58 | -3.35 |
| $z_*$ [AU] | 0.68 | 0.25 | 0.27 | 0.29 |

Table 3.3: MCMC results for density structural parameters. This includes the max likelihood value for each parameter, as well as the values for the 16th, 50th and 84th percentiles.

results. Table 3.3 lists the max likelihood for each parameter, as well as the values for the 16th, 50th (median), and 84th percentiles. The resulting corner plot can be seen in Figure A.1 located in the Appendix.

The results show that the star's position in the z-direction is very close to zero. This makes sense, as this should be mainly constrained by the inclination of the disk. Because there is still a slight offset in this direction, this is accounted for by the fact that Lagrange et al. (2016) found the inclination to be 85.4+/- 0.1, slightly higher than our estimated value of 85.07 degrees. On the other hand, the offset in the x-direction is much more significant, as this is what would cause a brightness asymmetry on either side of the disk. The MCMC analysis favors a stellar offset approximately 3.58 AU towards the SE extension of the disk, which is also the brighter side. This amount of offset, while not very large, is enough to cause the SE extension to be brighter than the NW extension by $\sim$1.07 within 0.34$''$ and by $\sim$1.15 times at a separation of 0.4$''$ to 0.5$''$. However, this is an underestimate compared to the brightness asymmetry derived from our data. In addition, this is a much smaller offset than the 16.13 AU derived from fitting the spine of the disk, which may explain the underestimate in brightness.

We then reran the MCMC analysis with the H-band data. However, this time, the density structural parameters were kept fixed, using the 50th percentile values obtained in the previous run. Instead, the dust grain parameters were allowed to vary over the limit priors defined in table 3.2. This analysis was run for approximately 13 days until the log likelihood was no longer noticeably changing. The results can be found in Table 3.4.

| Param. | Max Lk. | 16% | 50% | 84% |
|---|---|---|---|---|
| $M_{dust}$ [$M_\oplus$] | 0.14 | 0.012 | 0.02 | 0.11 |
| porosity | 0.179 | 0.018 | 0.102 | 0.29 |
| $V_{Si}$ | 0.898 | 0.187 | 0.557 | 0.916 |
| $V_{aC}$ | 0.036 | 0.106 | 0.499 | 0.873 |
| $V_{H_20}$ | 0.797 | 0.042 | 0.241 | 0.828 |
| $a_{min}$ [$\mu$m] | 0.77 | 0.91 | 3.17 | 3.72 |
| $a_{exp}$ | 2.99 | 2.99 | 3.19 | 3.30 |

Table 3.4: MCMC results for dust grain parameters for H-band only. This includes the max likelihood value for each parameter, as well as the values for the 16th, 50th and 84th percentiles.

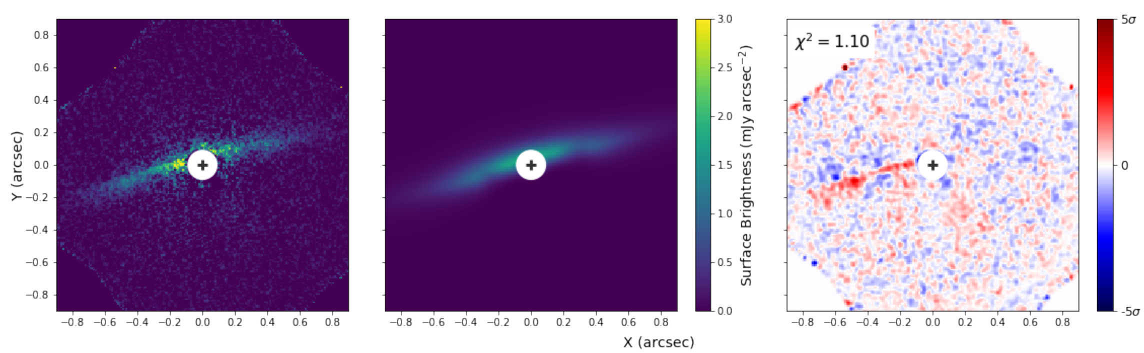


Figure 3.1: Results from modelling the whole disk with H-band only. **Left:** H-band data. **Middle:** Best fitting model. **Right:** Residual between data and best fitting model.

In this case, due to the bi-modal features seen in the majority of parameters, the max likelihood values for the dust grain properties are taken. These values, along with the median density structural values, are used to create a best fitting model. This can be seen in Figure 3.1, where the left plot is the H-band data, the middle plot is the best fitting model, and the right plot is the residual. The model fits the NW extension very well, with no visible residuals. However, there is a slight residual along the entire SE extension of the disk, where the model under-predicts the data. The interpretation of this is that, either our model is under-predicting the stellar offset as implied from our spine fitting, or there may be a difference in dust grain properties between the two sides.

| Param. | Max Lk. | 16% | 50% | 84% |
|---|---|---|---|---|
| $M_{dust}$ [$M_{\oplus}$] | 0.014 | 0.012 | 0.014 | 0.017 |
| porosity | 0.34 | 0.21 | 0.35 | 0.39 |
| $V_{Si}$ | 0.006 | 0.001 | 0.038 | 0.128 |
| $V_{aC}$ | 0.99 | 0.95 | 0.98 | 0.99 |
| $V_{H_20}$ | 0.16 | 0.001 | 0.04 | 0.4 |
| $a_{min}$ [$\mu$m] | 1.71 | 1.53 | 1.54 | 1.70 |
| $a_{exp}$ | 3.06 | 3.05 | 3.061 | 3.067 |

Table 3.5: MCMC results for dust grain parameters of the SE extension, using all three filters. This includes the max likelihood value for each parameter, as well as the values for the 16th, 50th and 84th percentiles.

### 3.3.2 All Bands

To explore this idea, we did an MCMC analysis of each side of the disk individually, to see whether or not different dust grain properties were favored. For these two runs, we include all three wavelengths in the hope of constraining the properties better than with the H-band alone. Again, we launch 200 walkers, and allow MCMC to run for approximately 19 days. Results can be found in Table 3.5.

Interestingly, modelling the SE extension only while using all three bands, yields very different results than modelling the entire disk with just the H-band alone. Here, the MCMC analysis favors a total dust mass an order of magnitude less than in our previous run. Additionally, the composition is radically different with a high volume fraction for amorphous carbon and very low volume fractions for astronomical silicate and water favored. While the previous run yielded a minimum dust grain size of 0.77 $\mu$m, this run yields a minimum dust grain size of approximately 1.71 $\mu$m. However, comparing the distribution of each parameter between these two runs, we find that modelling all three wavelengths improved the constraint of each parameter greatly. The resulting best fit models, taken from the maximum likelihood values, versus our data and residuals can be seen in Figure 3.2.

Finally, we modelled the fainter extension using all three bands, using the same process as with the SE extension. Results for this can be found in Table 3.6. The resulting best fit models, using the maximum likelihood values, and residuals for the NW can be seen in Figure 3.3. The reduced chi-squared values for each residual were calculated using Equation (3.5), where $O_i$ is our data, $C_i$ are our models and $\sigma_i$ represents the noise in the data. Finally, $\nu$ is the degree of freedom, which is given

| Param. | Max Lk. | 16% | 50% | 84% |
|---|---|---|---|---|
| $M_{dust}$ [$M_\oplus$] | 0.02 | 0.003 | 0.04 | 0.06 |
| porosity | 0.45 | 0.10 | 0.89 | 0.92 |
| $V_{Si}$ | 0.12 | 0.01 | 0.14 | 0.78 |
| $V_{aC}$ | 0.63 | 0.52 | 0.74 | 0.96 |
| $V_{H_20}$ | 0.37 | 0.01 | 0.08 | 0.35 |
| $a_{min}$ [$\mu$m] | 0.77 | 1.08 | 1.13 | 3.02 |
| $a_{exp}$ | 3.17 | 2.73 | 2.78 | 3.90 |

Table 3.6: MCMC results for dust grain parameters of the NW extension, using all three filters. This includes the max likelihood value for each parameter, as well as the values for the 16th, 50th and 84th percentiles.

by the number of observations minus the number of fitted parameters.

$$\chi^2_\nu = \frac{1}{\nu}\sum_i \frac{(O_i - C_i)^2}{\sigma_i^2} \tag{3.5}$$

## 3.4 Summary

We use the 3-D radiative transfer code, MCFOST, to model HD 106906's debris disk. Additionally we use the Python package *emcee*, which utilizes MCMC, to explore the given parameter space, in the hopes of better constraining the disks density structural and dust grain properties. We first go through this process with only the H-band data, as it has the highest S/N. By doing so, we are able to constrain the disk's density structural parameters and find a well fitting model; however, the dust grain parameters are not well constrained. The MCMC analysis also favours a stellocentric offset of ∼3.58 AU towards the SE extension, although a residual still remains in this side, suggesting that either the offset is being underestimated or is not enough to account for the brightness asymmetry. To test this, we modelled both sides of the disk individually to see whether or not there is a difference in dust grain properties, where we also include all three wavelengths. Doing so, we are able to better constrain the dust grain parameters on both sides, compared to the initial run, as well as we find several differences between the two sides. These differences will be discussed in more detail in the following chapter.

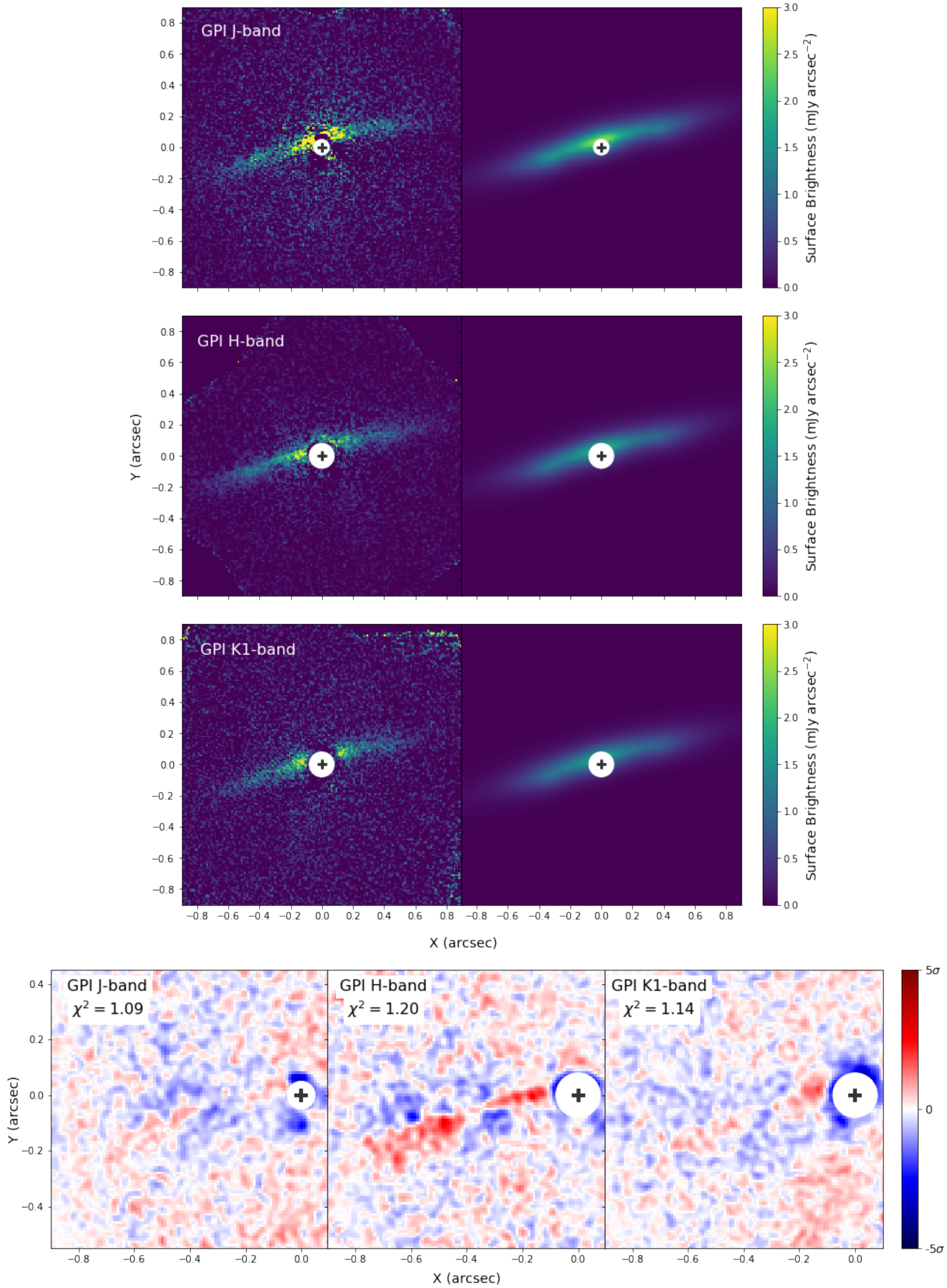


Figure 3.2: Resulting best fit models from modelling the SE extension with all three wavelengths. **Top Left:** Polarimetric data. **Top Right:** Best fitting models. **Bottom:** Residuals from best fit models of SE extension in J-, H- and K1-band.

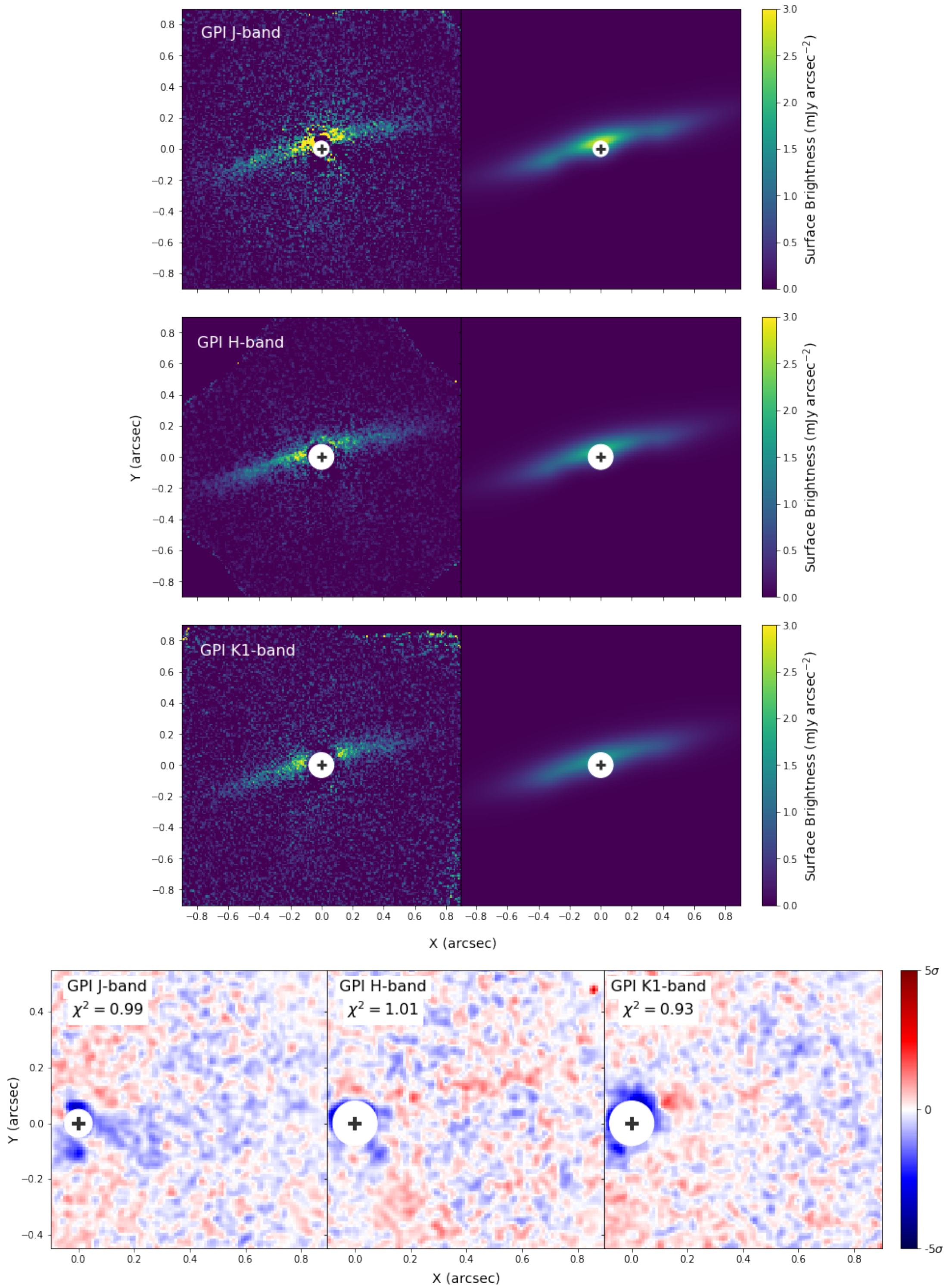


Figure 3.3: Resulting best fit models from modelling the NW extension with all three wavelengths. **Top Left:** Polarimetric data. **Top Right:** Best fitting models. **Bottom:** Residuals from best fit models of NW extension in J-, H- and K1-band.

# Chapter 4

# Discussion

## 4.1 Disk Structure

From our MCMC modelling, we obtain a scale height $H_0$ of $4.34^{+0.04}_{-0.03}$ AU with a vertical profile exponent of $\gamma = 0.715^{+0.01}_{-0.01}$. Comparing $H_0$ to previous work, our value of 4.34 AU is much larger than the 0.5 AU set in Lagrange et al. (2016) based on total intensity SPHERE data. This is expected, as methods used to subtract the effects of the star in total intensity are more likely to result in strong subtraction of the disk emission as well. Polarimetric images result in a better representation of the width of the disk because PSF subtraction is not needed to remove the stellar emission, which is inherently unpolarized.

We also obtain a critical radius $R_c = 72.21^{+3.10}_{-3.30}$ AU, signifying the change from $\alpha_{in}$ to $\alpha_{out}$, where we find $\alpha_{in} = 1.03^{+0.29}_{-0.24}$, and $\alpha_{out} = -2.26^{+0.11}_{-0.08}$. This means that the surface density of the disk increases from $R_{in}$ to $R_c$, at which it then begins to decrease. Again, we compare our results to Lagrange et al. (2016), where our measured $\alpha_{in}$ is much less than the $\alpha_{in} = 10$ that is used to model the SPHERE data. This also results in different measured values of $\alpha_{out}$, with our value of -2.26, compared to -4 derived by Lagrange et al. (2016).

Finally, we included a stellocentric offset in our modelling, defined as $x_*$ and $z_*$, where we obtain an offset of $-3.56^{+0.23}_{-0.05}$ AU and $0.27^{+0.02}_{-0.03}$ AU. Moving the star 3.56 AU towards the SE extension causes a small brightness asymmetry in the disk, but not enough to account for the total brightness asymmetry, as can be seen in Figure 3.2, where there are lingering residuals in the SE extension from modelling the entire disk with the H-band. In addition, this offset is much smaller than the x-offset of 16.13

AU derived from fitting the spine of the disk, which may explain the discrepancy in surface brightness. This could be due to the fact that, at the same time, we do not measure an asymmetry in the radial extent, which may be why MCMC prefers a smaller stellocentric offset, incapable of matching the brightness of the SE extension. Increasing the offset would cause one side of the disk to be extended, while the other side would become truncated, creating a disk structure that does not match the data. This discrepancy shows some of the limitations of our model, which will be further discussed in Section 4.4, where the circular model structure may not be appropriate for this particular disk, and may require a more complicated and eccentric model.

## 4.2 Dust Grain Properties

When modelling the entire disk using the H-band only, we get a good fitting model with a reduced chi-squared of 1.10. However, the majority of dust grain parameters are not well constrained, and there remains a significant residual in the SE extension. By modelling each side individually, across all three wavelengths, we have been able to better constrain the dust grain parameters. This has allowed us to compare the dust grain properties between the SE and NW extensions.

For the SE extension, we obtain a total dust mass of $0.014^{+0.003}_{-0.002}$ $M_{\oplus}$, as well as a porosity of $0.35^{+0.04}_{-0.14}$. We find a composition dominated by amorphous carbon with a volume fraction of $0.98^{+0.01}_{-0.03}$, while the volume fractions for water ice and astronomical silicate are close to zero. For the minimum dust grain size, we obtain a probability distribution of $1.54^{+0.16}_{-0.01}$ $\mu$m and a maximum likelihood of 1.71 $\mu$m, with a dust size distribution exponent of $3.06^{+0.01}_{-0.01}$. Looking at the residuals in each band, we still see a significant residual in the H-band, closest to the star as well as towards the outer edge of the disk. The residual towards the outer edge may be due to higher back scattering in the data compared to the model, however, this would not be the case within the inner ring close to the star. In this case, the inability to model the brightness in the SE extension near the star could again be due to the limitations of our model, suggesting the need for a more complicated and eccentric model.

In comparison, we find a total dust mass of $0.04^{+0.018}_{-0.037}$ $M_{\oplus}$ for the NW extension, with a maximum likelihood of 0.20 $M_{\oplus}$. While the total dust mass for the SE extension is within the derived NW dust mass range, a higher total dust mass for the NW extension is favored despite being the fainter side, however it is not well constrained. For porosity we find a probability distribution of $0.90^{+0.02}_{-0.079}$ with a maximum likelihood of 0.45. For dust composition, we find $V_{Si} = 0.14^{+0.64}_{-0.13}$, $V_{aC} = 0.74^{+0.23}_{-0.21}$ and $V_{H_20} = 0.08^{+0.27}_{-0.07}$, while the maximum likelihood values differ slightly from the median values, with $V_{Si} = 0.12$, $V_{aC} = 0.63$, and $V_{H_20} = 0.37$. Compared to the SE extension, the NW extension is favored to have less amorphous carbon with a higher fraction of silicate and water ice. Also interestingly, MCMC favors a minimum dust grain size of 0.77 $\mu$m, which is half that of the minimum dust grain size in the SE extension, however, this is outside the derived probability distribution of $1.13^{+1.89}_{-0.05}$ $\mu$m. In addition, we get a $a_{exp}$ with a maximum likelihood of 3.17 and a probability distribution of $2.78^{+1.12}_{-0.05}$. While these dust grain properties are better constrained than when modelling the H-band alone, we note that some of these parameters still have large distributions with more than one peak, as can be seen in Figures A.3 and A.4. Because of this, we chose the maximum likelihood values to compare and contrast the dust grains of the SE and NW extensions, as these values create the best $\chi^2$ models.

Assuming a combined mass of 2.71 $M_\odot$ for HD 106906AB (Rodet et al. 2017), and a luminosity of $6.56 \pm 0.04$ $L_\odot$ (Gaia Collaboration et al. 2018), we can approximate the blowout size ($a_{\rm blow}$) for this system (Pawellek & Krivov 2015; Burns et al. 1979). Doing so, we get an $a_{\rm blow}$ of $\sim$0.85 $\mu$m. This means that any dust grains below this size should be blown out of the disk by radiation pressure from the central binary. One reason why we might see a smaller grain size in NW extension could be due to a recent collision, where the smaller dust grains have not yet had the chance to be blown out of the system.

The scenario of a recent collision may also be supported by the increase in water ice, as well as the increase in $a_{exp}$ and $M_{dust}$. A similar result was found for HD 111520, another debris disk which exhibits a brightness asymmetry. In that case, modelling showed one side of the disk to have a smaller minimum dust grain size than $a_{\rm blow}$, as well as an increase in water ice, $a_{exp}$ and $M_{dust}$ (Draper 2018), leading to an interpretation that there may have been a recent large collision between two icy bodies. However, with the case of HD 111520, the side where this collision was expected to take place was found to be two times brighter than the other side. The fact that the NW extension for HD 106906 is dimmer than the SE, makes this scenario seem unlikely.

Another explanation is that the disk indeed has an eccentricity as suggested from our spine fitting. This would cause the disk to have two different blowout sizes at the periastron and apastron (Murray & Dermott 1999), where periastron is the side of an eccentric disk that is closest to the star and apastron is the side of the disk that is farthest from the star. In this case, due to the difference in radiation pressure, the apastron would have a smaller blowout size and vice versa. Additionally, M. Kim et al. (2018) found that increasing the dynamical excitation of dust grains in a debris disk gave rise to a greater amount of smaller grains on the apastron side. They also found that the material strength for collisions also affects the amount of smaller dust grains on either side. For reference, material strength determines the amount of impact energy per unit of target mass (specifically for smaller objects with D $<$ 0.1 km) needed to create a fragment 50% the mass of the original target. This is because the material strength helps determine the number of destructive collisions in a disk, where more destructive collisions leads to a build up of small grains on the apastron side given the longer orbital timescales at this location.

Both of these parameters affect what is known as the "Pericenter Glow", where the the apocenter-to-pericenter flux ratio is less than 1, as in the case for HD 106906. From M. Kim et al. (2018), given an eccentricity of 0.4, along with a material strength of $5 \times 10^2$ J/kg gives a similar apocenter-to-pericenter flux ratio to the brightness asymmetry we observe (0.78-0.86) at a wavelength of $\sim$1-3 $\mu$m, although the location of the apocenter and pericenter of our disk would need to be confirmed to know the exact flux ratio. Additionally, having an eccentricity and dynamical excitation of $0.4 \pm 0.1$ can also lead to a similar apocenter-to-pericenter flux ratio. This shows that in order to match the difference in surface brightness for an eccentric disk, the dynamical excitation of dust grains as well as the material strength are important to consider, as too low of a material strength or too high of a dynamical excitation can actually lead to an Apocenter Glow. As both these phenomenon vary with wavelength, mm-wavelength observations would be important in comparing the brightness asymmetry with our near-IR observations.

Porosity could also be a factor in considering the difference in minimum dust grain size. F. Kirchschlager and S. Wolf (2013) showed that increasing the porosity of dust grains in the disk, also increased $a_{\mathrm{blow}}$ depending on stellar type and temperature. Using a porosity of between 0.34 and 0.45 and a stellar temperature of 6484 K, yields an $a_{\mathrm{blow}}$ of 1.53-1.93 $\mu$m. This value better aligns with the minimum dust grain size 1.71 $\mu$m in the SE extension, but still doesn't explain the minimum dust grain size of 0.77 $\mu$m in the NW extension.

Additionally, composition needs to be taken into account. The blowout size of 0.89 $\mu$m was calculated assuming a pure astrosilicate composition with a density of 3.3 g/cm$^3$. This seems to be a poor assumption for this disk, given that the MCMC analysis favors a composition of mostly amorphous carbon, with some water ice and astrosilicate on both sides. Given an F6V type star with a surface temperature of 6250 K, and a disk with composition of 95% aC and 5% $H_20$, Arnold et al. (2019) found a blowout size of 1.4 $\mu$m using Mie compact grains. Adding in porosity, this value is even higher. They found the same blowout size of 1.4 $\mu$m for a composition of equal parts Si, aC and $H_20$, meaning that decreasing the relative amount of aC while increasing $H_20$, as we see in the NW compared to the SE, most likely won't change the blow out size dramatically, if at all for compact grains.

Taking all of these factors into account, while composition and porosity would affect the blowout size for this system, neither of these parameters differ enough across the disk to explain the minimum dust grain of 0.77 $\mu$m in the NW extension. The disk must have an eccentricity, leading to different blowout sizes, and therefore one side having a greater amount of smaller grains. This being said, the dust grain properties derived for this disk should be taken with a grain of salt given poor constraints for some of the parameters, as well as the limitations of our model discussed so far and further in Section 4.4.

## 4.3 Dynamical Interaction with HD 106906b

In this section, we compare our results to previous simulation work, both on HD 106906 specifically, as well as general disk-planet interaction studies.

The empirical analysis of our data supports a large eccentricity; this could be due to interaction with HD 106906b, either as it was ejected from the disk, or due to secular orbital effects. There are two papers that look into this using particle simulations (Nesvold et al. 2017; Rodet et al. 2017). While Rodet et al. (2017) examines the morphological outcomes of the disk from both the planet being ejected and from secular effects, Nesvold et al. (2017) examines solely the secular effects.

Rodet et al. (2017) found that the ejection of the planet from the disk was able to reproduce the asymmetries on larger scales, as seen with HST, where particles are blown out to high eccentricities on the right side of the disk. However, the ejection was not able to reproduce the NW/SE asymmetry on smaller scales as seen with GPI. On the other hand, the affect of the planet on a eccentric, inclined orbit, was able to reproduce the smaller scale asymmetries with a larger density in the SE than the NW. This also gives rise to a needle-like structure at larger distances, but not as strongly as the ejection scenario, suggesting that the two effects together could explain the observations on large and small scales.

In contrast, Nesvold et al. (2017) did a more in depth look at the affect on the disk from the planet initially located at 700 AU (In Situ) with an adopted eccentricity of 0.7, as it orbits at different inclinations. Through this alone, they were able to recreate both the small and large scale asymmetries, where a needle like structure was seen up to 500 AU, while closer in the SE extension is brighter than the NW extension. One caveat is that this model predicts a greater brightness asymmetry than we observe with GPI, particularly past 50 AU where the NW/SE ratio from their simulation is ~0.4 compared to 0.8 derived from our H-band. This simulation also predicts an induced eccentricity of ~0.3, which is much larger than the offset predicted with MCMC, but better aligns with the large eccentricity derived with the spine fitting. However, for this simulation, an eccentricity of 0.3 additionally creates a radial length asymmetry where the SE extension extends to ~90 AU, while the NW extension extends past 100 AU (See Figure 4.1(a)), where we detect no such radial asymmetry with our data. This could be because our near-IR observations track mainly the distribution of micron-sized dust grains, while sub-micron dust grains have been shown by HST to have a radial asymmetry.

In a more general case, Lee and Chiang (2016) look at a number of different debris disk morphology's, including the "Needle", which is described as eccentric and vertically thin disk viewed edge on, such as with HD 106906. In their analysis, they find that along with a radial length asymmetry, where one side extends much farther than the other, there is also a brightness asymmetry. In this case, the shorter side of the disk is brighter closest to the star, but eventually at larger distances, the longer side becomes brighter. This is consistent with the previous simulations, as well as the GPI/HST observations to a degree, although this model also predicts a more dramatic brightness asymmetry within 100 AU.

While all of these models and simulations predict radial and brightness asymmetries that are consistent with our data plus HST observations, there is one inconsistency, namely that the brightness asymmetry is much more dramatic than we see in our GPI observations. Along with a dramatic brightness asymmetry, the disk should also have a large eccentricity, as derived in Nesvold et al. (2017). While our modelling is incapable of showing this, our empirical analysis of the data shows evidence that there is a large disk eccentricity, which in turn, may have been have been induced by HD 106906b. In the context of dust grain properties, none of these works look more closely at the changes in the specific dust grain properties themselves. Therefore, we

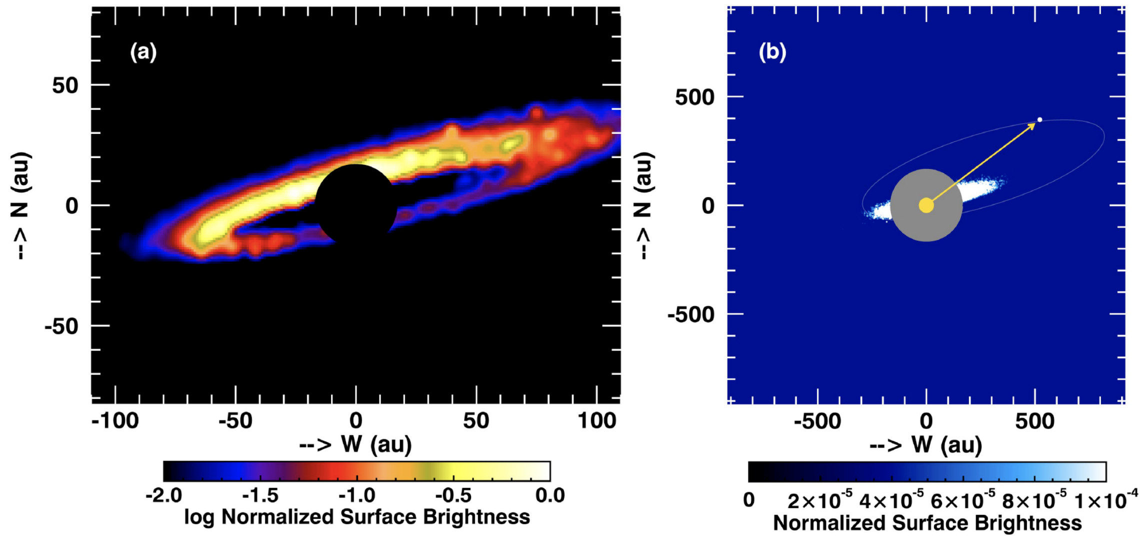


Figure 4.1: SMACK Simulation results for HD 106906 planet/disk interactions after 5Myr and a planet semi-major axis of 700 AU, eccentricity=0.7, and inclination=8.5°. **(a):** Recreation of SPHERE near infrared observations from Lagrange et al. (2016), Figure 1. **(b):** Recreation of HST optical observations from Kalas et al. (2015), Figure 3. This figure is taken from Nesvold et al. (2017) with permission.

cannot compare our dust grain results, other than the difference in $a_{min}$ caused by an eccentric disk, in terms of dynamical interaction with the planet. More simulation work for this system will need to be done to probe further the affect this type of interaction will have on specific dust grain properties such as porosity, composition, and the distribution of dust grain sizes.

## 4.4 Limitations

There are several limitations with our MCFOST models that could impact our results. The first is that our models did not have an inherently eccentric disk. While we are able to offset the star, the disk remains circular, which would not be the case for a truly eccentric disk. This may be why our modelling predicts only a very small offset and is unable to match the brightness of the SE extension. In this case, a custom density distribution would be needed, which could then be used within MCFOST in order to have a truly eccentric model. Another limitation is that our models assume a smooth dust mass distribution defined with only one power-law, which is not necessarily realistic, as certain sizes of dust grains may be missing or the distribution may have more than one power-law (Strubbe & Chiang 2006). Data from the Atacama Large

Millimeter/submillimeter Array (ALMA) would be useful in this case to constrain the dust mass distribution with millimeter observations, which again could be used within MCFOST to create a more realistic model.

A third limitation comes from the use of Mie theory in our models. As mentioned before, Mie theory uses compact spherical grains, which makes computations much faster and easier, but is unrealistic. In reality, dust grains are not perfectly spherical, but are rather irregularly shaped aggregates. This may strongly affect the accuracy of our results for the dust grain properties, as they rely heavily on this assumption and how light is scattered. For example, Min et al. (2015) found the scattering phase function differed for Mie dust grains and realistic aggregates for scattering angles greater than 90 degrees (backside of the disk). Where for Mie grains the phase function generally decreased, on the other hand, they found for aggregates that the phase function either increased or stayed flat. Another example is the affect this has on the blowout size, where Arnold et al. (2019) calculated $a_{\mathrm{blow}}$ for aggregates with porosity of 76.4%, and found that, in general, it was 2-3 times higher than for Mie compact grains. While we leave more complex modelling with custom density/dust mass distributions and realistic aggregates for future work, these limitations show how it's important to not rely too heavily on modelling, and instead focus more on the empirical analysis of the data.

## 4.5 Debris Disk Comparison

We can compare HD 106906's morphology to other debris disks with similar morphology's. While HD 106906 can be considered very unique, being one of only a handful disks with a know disk and planet companion, the morphological features of this disk itself can be seen in several other systems.

This includes disks such as HD 32297, HD 61005, and HD 15115. Not only do all of these disks have similar inclinations (near edge on), but they also have extended halos as imaged with HST (Schneider et al. 2014). In addition, HD 61005 and HD 15115 present brightness asymmetries on smaller scales similar to HD 106906. However, while there may be more compelling evidence of a stellocentric offset with HD 61005, large eccentricities in all three systems have not yet been detected (Mazoyer et al. 2014; MacGregor et al. 2018).

The initial explanation for the features in these disks were interactions with the interstellar medium (ISM, Debes et al. 2009). By passing through a dense cloud of interstellar gas, this causes specifically small grains to be stripped from the disk into the halo due to ram pressure. This may result in the ”wing” feature for HD 32297 and HD 61005, as well as the ”needle” feature for HD 15115 and HD 106906, depending on the angle of the interaction with the ISM.

This explanation changed for HD 32297 and HD 61005, however, after obtaining ALMA observations. While ISM interactions only affect small grains, MacGregor et al. (2018) found that the larger grains were also populating the halo for these two disks. This ruled out the ISM scenario, in favor of other scenarios such as sculpting due to planet perturbations, although no planets have been detected thus far. On the other hand, ALMA did not show this same effect with HD 15115 (MacGregor et al. 2019), indicating that the ISM scenario may still be the best explanation for this disks morphology.

HD 32297 and HD 61005 show that it may be possible to have an extended halo due to planet interactions. Although, an interaction with the ISM may also explain these features as seen with HD 15115. This explanation may be reasonable for HD 106906 as the needle feature has only been observed in the optical with HST, and was not detected in near infrared observations with SPHERE, suggesting that only very small dust grains populate the halo. However, the proper motion of HD 106906 is perpendicular to the disk, where for an ISM interaction we would expect a proper motion in the opposite direction of the needle structure, making this scenario less likely. With a known planet companion and empirical evidence of a large disk eccentricity, a planet-disk interaction is still the most probable scenario. Although, high resolution ALMA data would still be useful to determine whether or not larger dust grains are detected in the halo which will provide a means of discriminating the exact origins of HD 106906’s asymmetries.

# Chapter 5

# Conclusion

With GPI, we have obtained polarimetric data of HD 106906's disk in H-band, as well as J- and K1-bands. With these data, we conclude the following:

1. The FWHM-profile in the H-band shows that the NW extension is slightly more vertically extended, with a weighted average of $0.12''$ compared to $0.11''$. The disk is also detected to an angular extent of $0.8''$ on both sides, indicating no strong asymmetry in this regard. In addition, we detect back scattering from the far side of the disk beginning at $\sim 0.34''$ on either side.

2. A brightness asymmetry is observed in all three wavelengths, where the asymmetry is detected out to $\sim 0.6''$. Within $0.34''$, the NW/SE brightness ratio is $0.80 \pm 0.37$ in the J-band, $0.75 \pm 0.22$ in the H-band and $0.82 \pm 0.31$ in the K1-band. At an angular separation of $0.4''$-$0.5''$, we detect a NW/SE brightness ratio of $0.70 \pm 0.30$ in the J-band, $0.80 \pm 0.21$ in the H-band and $0.78 \pm 0.32$ in the K1-band.

3. To get a deeper look into the disk structure, we fit the spine of the disk using a simple, inclined ring model. Doing so, we derived the following; $R_d = 72.70^{+2.55}_{-1.29}$ AU, $i = 85.07^{+0.15}_{-0.16}$ degrees, and PA $= 103.67^{+0.16}_{-0.30}$ degrees, where the inclination and PA are consistent with those derived in Kalas et al. (2015). We also find a large x-offset of $= 16.13^{+2.73}_{-1.27}$ AU and a y-offset of $= -2.52^{+0.22}_{-0.32}$ AU towards the SE extension, indicating a large eccentricity approaching $\sim 0.5$. While further analysis is needed to probe this eccentricity further, this suggests that the disk structure truly is asymmetric.

4. Using MCFOST and MCMC, we were able to model the disk and constrain certain parameters. By modelling the H-band separately, as it has the highest S/N, we were able to well constrain its density structural properties, such as $\alpha_{in}$ and $\alpha_{out}$ which we find to be much smaller than predicted in Lagrange et al. (2016). Our modelling also suggests a much smaller stellar offset of $\sim$3.58 AU than we derive from our spine fitting, which may be due to the limitations of our non-eccentric model.

5. By modelling both sides of the disk individually, we were able to better constrain the dust grain properties, and compare the results to each other. We find that our models favor a NW side with a higher dust mass, higher porosity, and a composition with slightly less aC and higher water ice. We also obtain a different minimum dust grain size of 0.77 $\mu$m for the NW extension compared to 1.71 $\mu$m for the SE extension. However, we still see a residual in the SE extension, which again may be due to physical limitations of our models.

6. The difference in the dust grain properties between the two extensions, more specifically the minimum dust grain size, could be due to a recent collision, or more likely an eccentric disk causing two different blowout sizes. In addition, considering a material strength for collisions and the dynamical excitation of dust grains can cause a similar apocenter-to-pericenter flux ratio that we see in our data. In terms of minimum dust grain and blowout sizes, it is important to note the role of porosity and composition can significantly impact these parameters; however, based on our modelling, these would not cause the observed difference in minimum dust grain sizes.

7. It is most probable that dynamical interaction with HD 106906b could have caused some of the features that we see in our data, such as the brightness asymmetry and eccentricity. However, the brightness asymmetry seen in previous works and simulations is predicted to be more extreme than we detect with GPI. More work would need to be done in order to look at the affects of such an interaction would have on more specific dust grain properties, such as porosity and the dust grain size distribution in order to be able to compare directly with our modelling results.

## 5.1 Future Work

Our results reveal further insights into the structure and asymmetries of the HD 106906 debris disk. While modelling can reveal further properties of debris disks, the evidence of a large eccentricity for HD 106906 would mean that our non-eccentric model is no longer appropriate, and may be the reason for the remaining residual seen in the SE extension. For future work, there are a few things that could be improved upon in our modelling. 1) Using a truly eccentric model with a custom density distribution. 2) Using a more realistic dust mass distribution. 3) Using a model that utilizes realistic aggregates would help shed light into the dust grain properties of the disk even further. In addition to improvements in modelling, future work is planned to continue our empirical analysis of the data, such as using an elliptic inclined ring model to fit the spine of the disk in order to probe the eccentricity further.

Obtaining high resolution data from ALMA will also be extremely useful in comparing the apocenter-to-pericenter flux ratio to near-IR observations, as well as the distribution of mm-sized grains will help inform whether the origin of the halo's needle architecture is due to an ISM interaction or in fact due to an interaction with HD 106906b.

# Appendix A

# Additional Information

## A.1 Corner Plots

Below are the corner plots from our modelling and MCMC analysis, using the Python package *corner* (Foreman-Mackey 2016). Figure A.1 shows the corner plot for modelling the density structural parameters with H-band only, while Figure A.2 shows the corner plot for modelling the dust grain properties with H-band only. Figure A.3 and Figure A.4 show the corner plots for modelling the dust grain properties of the SE and NW extensions individually, using all three wavelengths.

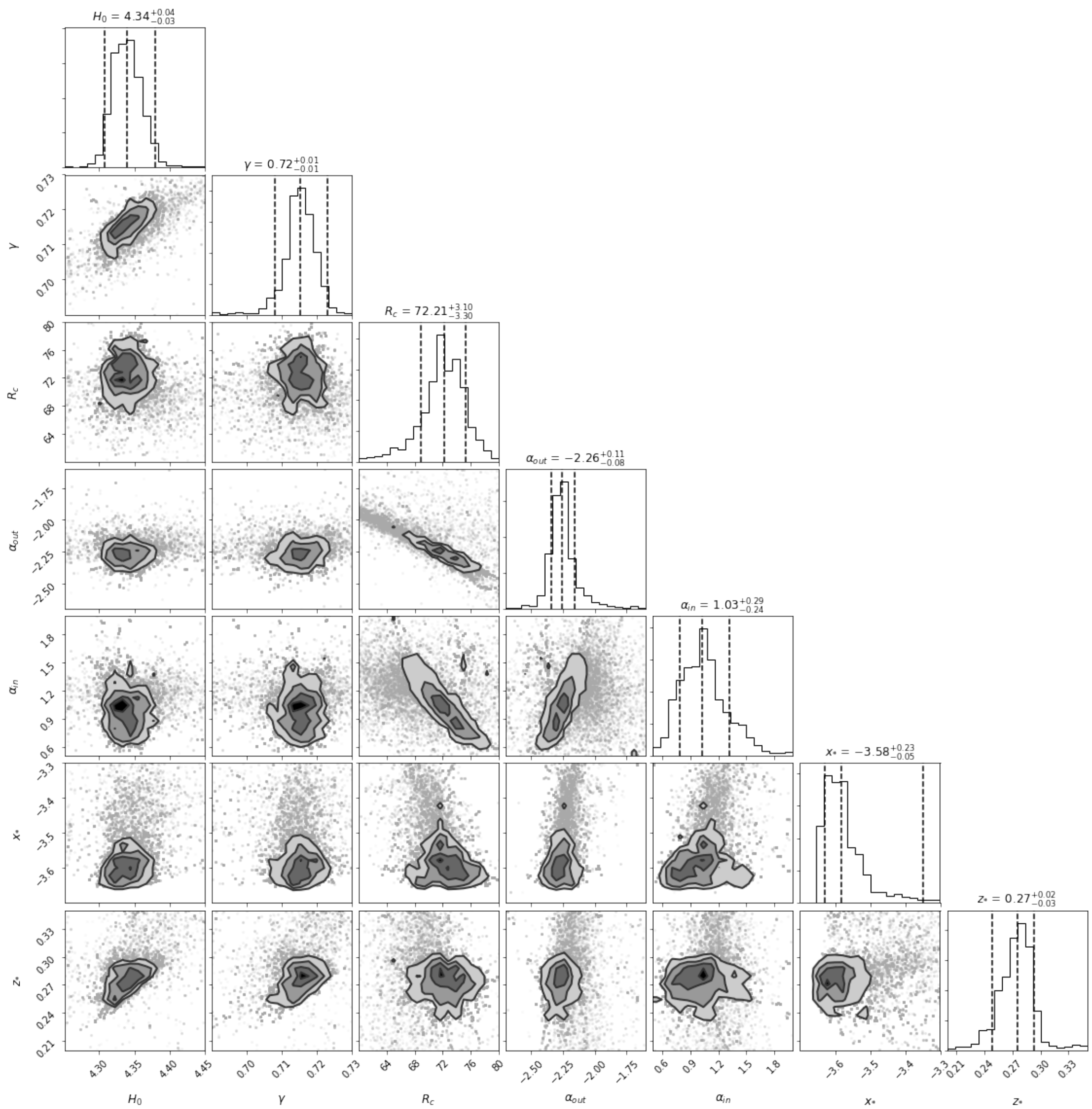


Figure A.1: Corner plot for MCMC results of density structural parameters.

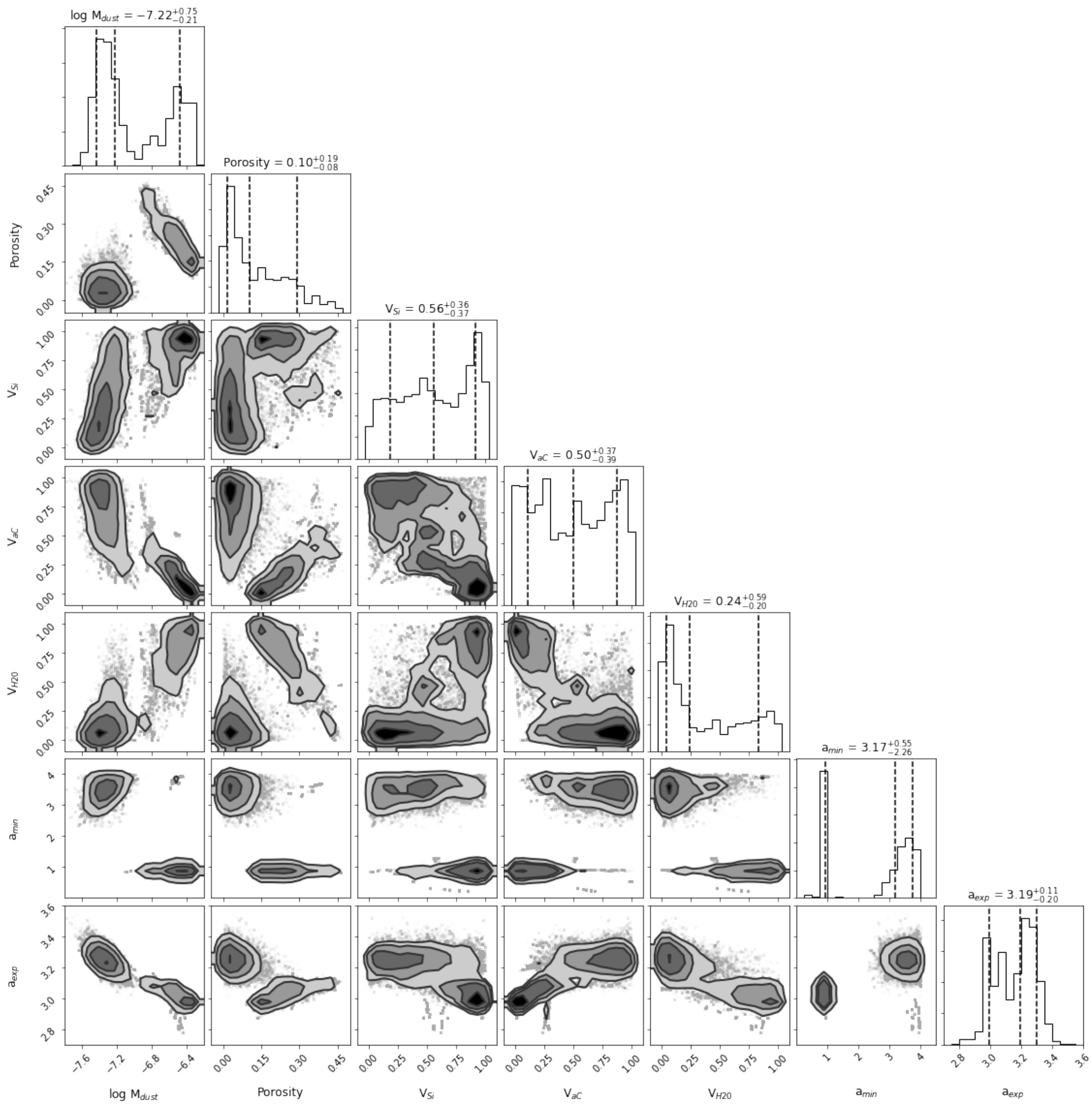


Figure A.2: Corner plot for MCMC results of dust grain parameters for H-band only.

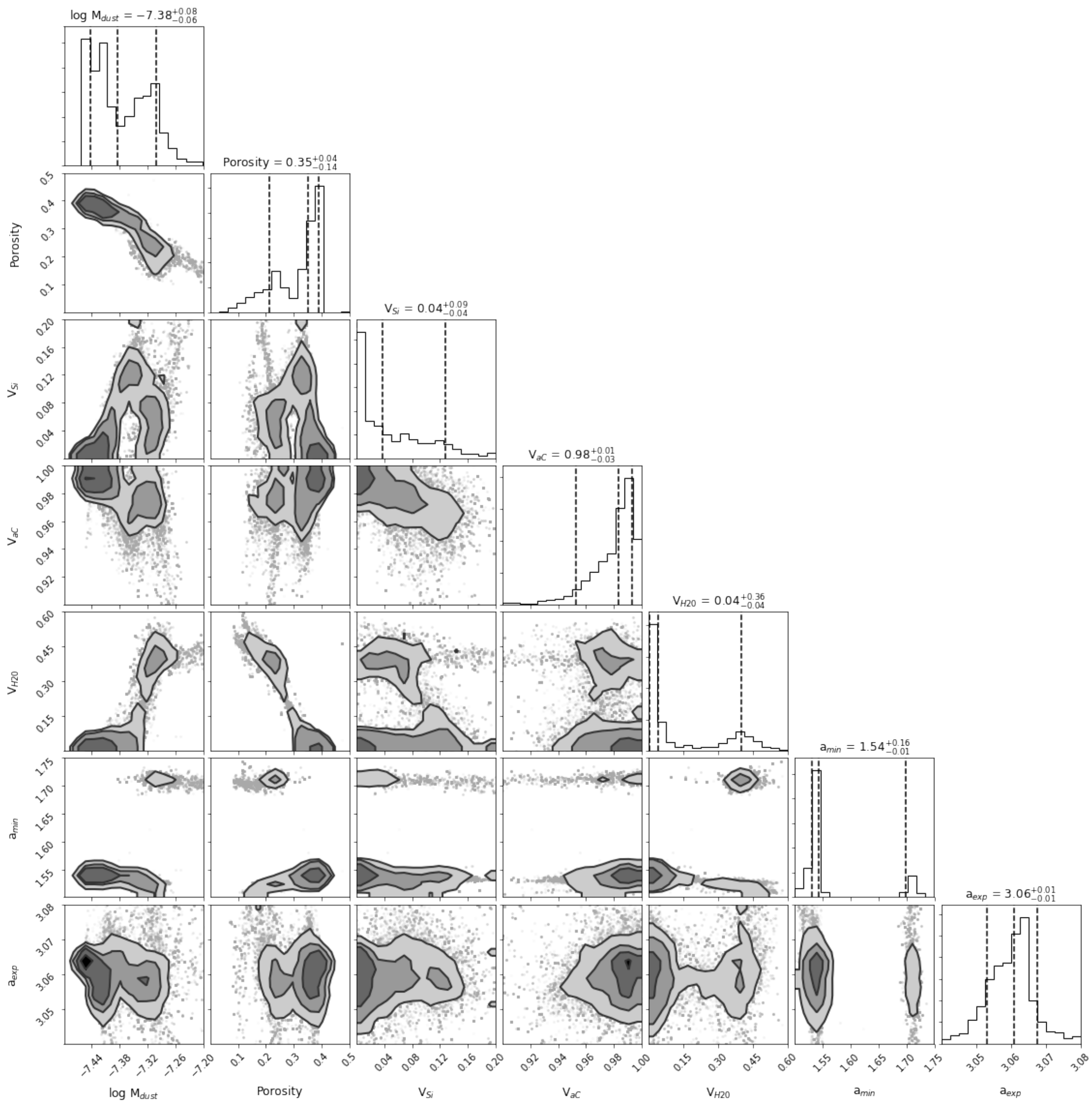


Figure A.3: Corner plot for MCMC results of dust grain parameters for SE extension using all three bands.

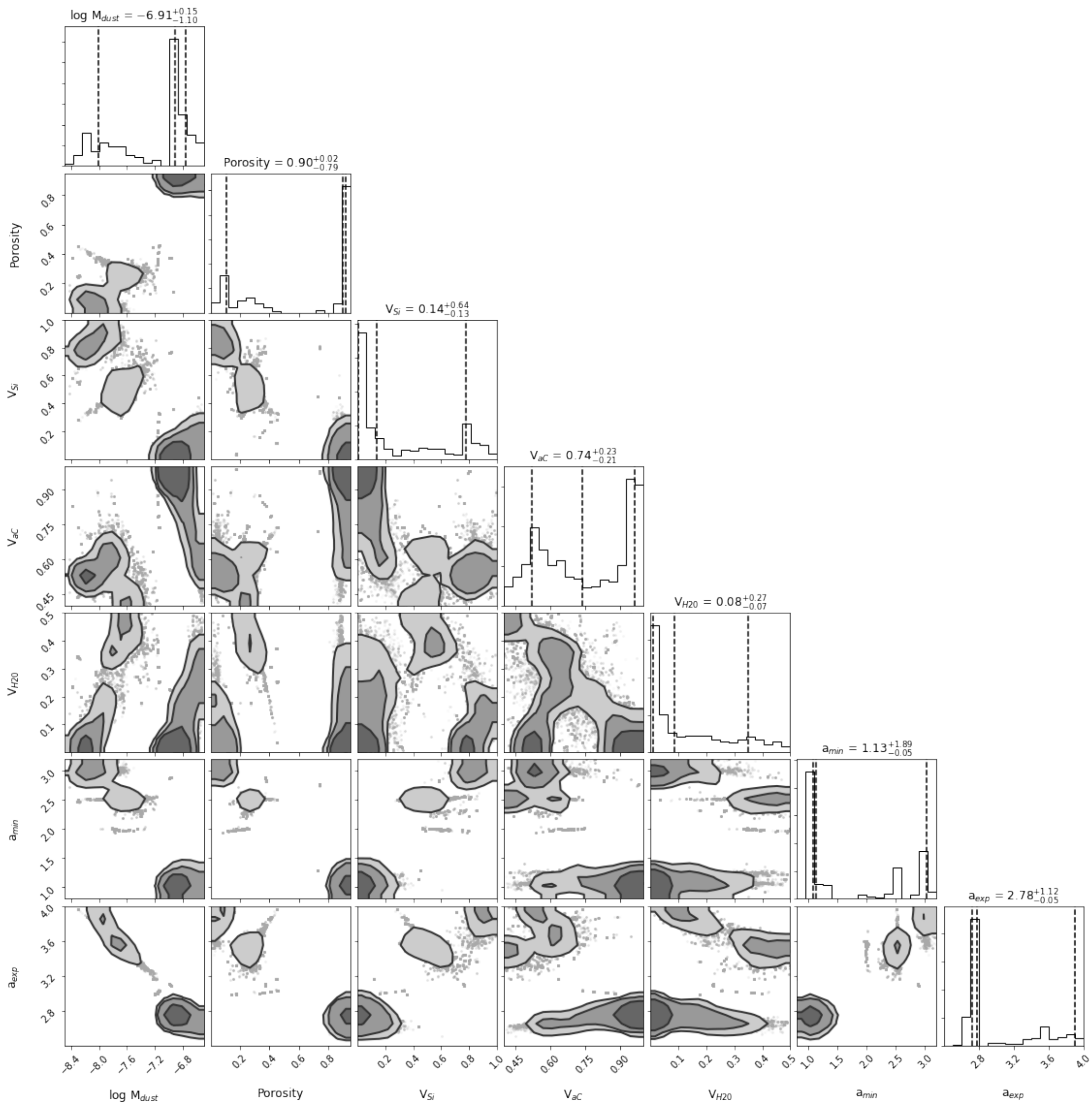


Figure A.4: Corner plot for MCMC results of dust grain parameters for NW extension using all three bands.

# Bibliography

Apai D., Schneider G., Grady C. A., Wyatt M. C., Lagrange A.-M., Kuchner M. J., Stark C. J., Lubow S. H., 2015, Astrophysical Journal, 800, 136

Arnold J. A., Weinberger A. J., Videen G., Zubko E. S., 2019, Astrophysical Journal, 157, 157

Augereau J. C., Lagrange A.-M., Mouillet D., Papaloizou J. C. B., Grorod P. A., 1999, Astronomy and Astrophysics, 348, 557

Bailey V., et al., 2013, Astrophysical Journal, 780, L4

Boss A. P., 1997, Science, 276, 1836–1839

Burns J. A., Lamy P. L., Soter S., Lamy P. L., Soter S., 1979, Icarus, 40, 1

Chen C., Jura M., Gordon K., Blaylock M., 2005, Astrophysical Journal, 623, 493

Daemgen S., Todorov K., Quanz S. P., Meyer M. R., Mordasini C., Marleau G.-D., Fortney J. J., 2017, Astronomy and Astrophysics, 608, A71

Dawson R. I., Murray-Clay R. A., Fabrycky D. C., 2011, Astrophysical Journal Letters, 743, L17

De Rosa R. J., Kalas P., 2019, Astronomical Journal, 157, 125

Debes J. H., Weinberger A. J., Kuchner M. J., 2009, Astrophysical Journal, 702, 318

Dent W. R. F., et al., 2014, Science, 343, 1490

Draine B. T., Lee H. M., 1984, Astrophysical Journal, 285, 89

Draper Z. H., 2018, PhD thesis, The University of Victoria

Esposito T. M., et al., 2020, Astronomical Journal, 160, 24

Foreman-Mackey D., 2016, Journal of Open Source Software, 1, 24

Foreman-Mackey D., Hogg D. W., Lang D., Goodman J., 2013, Publications of the ASP, 125, 306

Gaia Collaboration Brown A. G. A., Vallenari A., Prusti T., de Bruijne J. H. J., Babusiaux C., Bailer-Jones C. A. L., 2018, Astronomy and Astrophysics, 616, A1

Hughes A. M., Duchene G., Matthews B., 2018, Annual Review of Astronomy and Astrophysics, 56, 541–591

Kalas P. G., et al., 2015, Astrophysical Journal, 814, 32

Kennedy G. M., Wyatt M. C., 2010, Monthly Notices of the RAS, 405, 1253–1270

Kennedy G. M., Wyatt M. C., Kalas P., Duchêne G., Sibthorpe B., Lestrade J. F., Matthews B. C., Greaves J. S., 2014, Monthly Notices of the RAS, 438, L96–L100

Kenyon S. J., Bromley B. C., 2008, Astrophysical Journal Letters, 179, 451

Keppler M., et al., 2018, Astronomy and Astrophysics, 617, A44

Kim M., Wolf S., Löhne T., Kirchschlager F., Krivov A. V., 2018, Astronomy and Astrophysics, 618, A38

Kirchschlager F., Wolf S., 2013, Astronomy and Astrophysics, 552, A54

Lagrange A.-M., et al., 2009, Astronomy and Astrophysics, 493, L21–L25

Lagrange A.-M., et al., 2012, Astronomy and Astrophysics, 542, A40

Lagrange A.-M., et al., 2016, Astronomy and Astrophysics, 586, L8

Lee E. J., Chiang E., 2016, Astrophysical Journal, 827, 125

Levison H. F., Kretke K. A., Duncan M. J., 2015, Nature, 524, 322

Li A., Greenberg J. M., 1998, Astronomy and Astrophysics, 338, 364

MacGregor M. A., et al., 2018, 2018, Astrophysical Journal, 869, 75

MacGregor M. A., et al., 2019, Astrophysical Journal Letters, 877, L32

Macintosh B., et al., 2014, Proceedings of the National Academy of Science, 111, 12661–12666

Matthews B. C., Krivov A. V., Wyatt M. C., Bryden G., Eiroa C., 2014, Protostars and Planets VI, 521

Mazoyer J., Boccaletti A., Augereau J.-C., Lagrange A.-M., Galicher R., Baudoz P., 2014, Astronomy and Astrophysics, 569, A29

Millar-Blanchaer M. A., et al., 2015, Astrophysical Journal, 811, 18

Min M., Rab C., Woitke P., Dominik C., Ménard F., 2015, Astronomy and Astrophysics, 585, A13

Mittal T., Chen C., Jang-Condell H., 2015, Astrophysical Journal, 798, 87

Müller A., et al., 2018, Astronomy and Astrophysics, 617, L2

Murray C. D., Dermott S. F., 1999, Solar System Dynamics. Cambridge University Press

Nesvold E. R., Kuchner M. J., 2015b, Astrophysical Journal, 798, 83

Nesvold E. R., Kuchner M. J., 2015a, Astrophysical Journal, 815, 61

Nesvold E. R., Naoz S., Fitzgerald M., 2017, Astrophysical Journal, 837, L6

Olofsson J., Juhasz A., Henning T., Mutschke H., Tamanai A., Moor A., Abraham P., 2012, Astronomy and Astrophysics, 542, A90

Ormel C. W., Klahr H. H., 2010, Astronomy and Astrophysics, 520, A43

Pawellek N., Krivov A. V., 2015, Monthly Notices of the RAS, 454, 3207–3221

Perrin M. D., et al., 2014, SPIE, 9147, 1168–1180

Pinte C., Menard F., Duchene G., Bastien P., 2006, Astronomy and Astrophysics, 459, 797

Ricci L., Carpenter J. M., Fu B., Hughes A. M., Corder S., Isella A., 2014, Astrophysical Journal, 798, 124

Rodet L., Beust H., Bonnefoy M., Lagrange A.-M., Galli P. A. B., Ducourant C., Teixeira R., 2017, Astronomy and Astrophysics, 602, A12

Rouleau F., Martin P. G., 1991, Astrophysical Journal, 377, 526

Schneider G., et al., 2014, Astrophysical Journal, 148, 59

Strubbe L. E., Chiang E. I., 2006, Astrophysical Journal, 648, 652

Vandenbussche B., et al., 2010, Astronomy and Astrophysics, 518, L133

Wang J. J., et al., 2014, SPIE, 9147, 1678–1692

Wang J. J., et al., 2016, Astronomical Journal, 152, 97

Williams J. P., Cieza L. A., 2011, Annual Review of Astronomy and Astrophysics, 49, 67